Article:
Benson, AP orcid.org/0000-0003-4679-9842, Stevenson-Cocks, HJ orcid.org/0000-0003-1044-3545, Whittaker, DG et al. (2 more authors) (2020) Multi-scale approaches for the simulation of cardiac electrophysiology: II - tissue-level structure and function. Methods. ISSN 1046-2023

https://doi.org/10.1016/j.ymeth.2020.01.010

Highlights

Multi-scale approaches for the simulation of cardiac electrophysiology: II - tissue-level structure and function

Alan P. Benson, Harley J. Stevenson-Cocks, Dominic G. Whittaker, Ed White, Michael A. Colman

- Computational models of the heart provide remarkable insight into cardiac function
- Equations for phenomenological and biophysical cellular excitation are presented
- Equations for propagation of excitation in 1, 2 and 3 dimensions are presented
- Methods for discretisation and integration of these equations are discussed
- Experimental methods for tissue model parameterisation and validation are discussed

Multi-scale approaches for the simulation of cardiac electrophysiology: II - tissue-level structure and function

Alan P. Benson[a,*], Harley J. Stevenson-Cocks[a], Dominic G. Whittaker[a,b], Ed White[a], Michael A. Colman[a]

[a]*School of Biomedical Sciences University of Leeds, Leeds LS2 9JT, UK*
[b]*School of Mathematical Sciences, University of Nottingham, Nottingham NG7 2RD, UK*

Abstract

Computational models of the heart, from **cell-level** models, through one-, two- and three-dimensional tissue-level simplifications, to biophysically-detailed three-dimensional models of the ventricles, atria or whole heart, allow the simulation of excitation and propagation of this excitation, and have provided remarkable insight into the normal and pathological functioning of the heart. In this article we present equations for modelling cellular excitation (i.e. the cell action potential) from both a phenomenological and a biophysical perspective. Hodgkin-Huxley formalism is discussed, along with the current generation of biophysically-detailed cardiac cell models. Alternative Markovian formulations for modelling ionic currents are also presented. Equations describing propagation of this cellular excitation, through one-, two- and three-dimensional idealised or realistic tissues, are then presented. For all types of model, from cell to tissue, methods for discretisation and integration of the underlying equations are discussed. The article finishes with a discussion of two tissue-level experimental imaging techniques – diffusion tensor magnetic resonance imaging and optical imaging – that can be used to provide data for parameterisation and validation of cell- and tissue-level cardiac models.

Keywords: cardiac tissue, electrophysiology, action potential, propagation, computational modelling

*Corresponding author
Email address: a.p.benson@leeds.ac.uk (Alan P. Benson)

1. Introduction

The physiological purpose of the heart is to function as a reliable, rhythmic pump to maintain the circulation of blood through the body for the duration of our life. Although the heart is a mechanical pump, this mechanical activity is driven by electrical activity through the process of excitation-contraction coupling [1–3]. During normal sinus rhythm, an electrical wave initiates in the sinoatrial node, then propagates through the two atria before being delayed at the atrioventricular node. The excitation wavefront then moves along the His-Purkinje conducting system before exciting the endocardial surfaces of the ventricles. The electrical wave then propagates transmurally towards the epicardial ventricular surface, exciting the entire ventricles. Thus the atria contract before the ventricles, with these two contractions forming the rhythmic cardiac cycle. If this normal rhythm is disturbed (a cardiac arrhythmia), electrical activity is no longer synchronised, mechanical activity therefore fails to synchronise, effective pumping of the blood ceases and death may occur.

The study of such arrhythmias has been a major focus of computational biology, as a detailed quantitative description of cardiac electrophysiology has been developed that allows the simulation of both normal and pathological excitation and propagation of this excitation [4, 5]. Additionally, the results of such simulations can be dissected in time and space, and by parameters, allowing a detailed study at the cell and tissue levels of the mechanisms underlying arrhythmias [6, 7]. Experimental studies of cardiac arrhythmias at the tissue level have been largely limited to voltage recordings on or near the surface of a preparation [8] or by using multiple plunge electrodes within the heart [9], and so computational studies offer an additional research tool. However, a model is, by definition, a simplification of a system, and so simulations are a trade-off between model complexity and computational efficiency, especially at the tissue and organ levels.

Nevertheless, models do not only describe physiological behaviour, they are predictive, and have provided remarkable insight into the normal and pathological functioning of the heart [10–17]. One focus of computational cardiac modelling is understanding the interaction between cell-level arrhythmia triggers (such as early and delayed afterdepolarisations) and tissue-level substrates (such as spatially heterogeneous refractory periods, or the myocyte disarray seen with pathologies such as heart failure) that enable these triggers to develop into re-entrant cardiac arrhythmias (e.g. [18–21]). Due

to technical and ethical limitations associated with animal and human experiments, computational models have played a crucial role in allowing us to understand these interactions.

Here we present monodomain equations and finite difference methods to simulate cell- and tissue-level electrophysiology (readers interested in other techniques such as bidomain equations and finite element methods are referred to references [4, 17, 22–24]). Although this article focusses on modelling cell- and tissue-level electrophysiology in ventricular tissue, the same principles apply to modelling electrophysiology in other types of cardiac cells and tissues (e.g. atrial [25]). This paper is Part 2 of a two-part article (see Colman et al. in this issue for Part 1); open-source code from the Leeds Computational Physiology Laboratory, covering the modelling presented in both parts of this article, is available in the Multi-scale Cardiac Simulation Framework from `http://www.physicsoftheheart.com/`.

2. Modelling Ventricular Myocyte Electrophysiology

Detailed mathematical and computational models of ventricular cell electrophysiology, constructed using experimentally obtained data and further validated against experimental results, provide tools for understanding excitation processes, both normal and abnormal, at the cellular level. The models reconstruct the ionic membrane currents and dynamic ion concentration changes that underlie the ventricular action potential, and form one component of the biophysically detailed models reconstructing propagation in the ventricles.

2.1. Ionic gradients; equilibrium and reversal potentials

The flow of an ion across the cell membrane through an open ion channel depends on the intra- and extracellular concentrations of that ion, and the membrane potential. Suppose that two reservoirs contain the same ion B but at different concentrations. Ion B has a positive charge. Each reservoir also contains another ion, S, with a negative charge and at concentrations such that each reservoir is, at least initially, electrically neutral. The two reservoirs are separated by a semi-permeable membrane that allows B to pass but not S. As the membrane is permeable to B, B will tend to move across the membrane down its concentration gradient. However, as S cannot cross the membrane there is a build up of negative charge in the reservoir from which B is moving. This build up of charge acts as an attracting force, opposing the movement

of B down its concentration gradient. The net gradient – i.e. the sum of the electrical and chemical gradients – is called the electrochemical gradient, and there comes a point when the force of the concentration gradient is exactly opposed by the force of the electrical gradient such that the electrochemical gradient is zero, and net movement of ion B through the membrane will stop. The voltage at which this occurs is known as the equilibrium potential, E_{eq} (or E_{B} for ion B), and is given by the Nernst equation

$$E_{\text{B}} = \frac{RT}{zF} \ln \left(\frac{[\text{B}]_{\text{o}}}{[\text{B}]_{\text{i}}} \right) \tag{1}$$

where $R = 8.314$ J.K^{-1}.mol^{-1} is the universal gas constant, T is absolute temperature (K), z is the valency of the ion, $F = 96485$ C.mol^{-1} is Faraday's constant, and $[\text{B}]_{\text{i}}$ and $[\text{B}]_{\text{o}}$ are the intra- and extracellular concentrations of ion B, respectively. For given intra- and extracellular ionic concentrations, an equilibrium potential exists for each ionic species. The electrochemical gradient for a particular ionic species is the difference between the membrane potential and the equilibrium potential, $V - E_{\text{eq}}$, and the sign of this gradient determines the direction of the flow of ions. Assuming that only one ionic species can flow across the membrane, the electrochemical gradient causes V to move towards E_{eq}. When $V = E_{\text{eq}}$ there will be no net flow, and changing V past E_{eq} will cause the electrochemical gradient, and therefore the direction of the flow of ions, to reverse.

Equilibrium potentials are not, however, properties of ion channels, although if a particular channel is only permeable to one ionic species, then the reversal potential, E_{rev}, of that channel (the potential at which there is no net flux through the open channel) will be the same as the equilibrium potential for that ion. However, channels are often permeable to more than one ionic species (the L-type Ca^{2+} channel, for example, which is permeable to Ca^{2+}, Na^{+} and K^{+}), and the reversal potential of the current in such cases will be the result of several equilibrium potentials. The Goldman-Hodgkin-Katz (GHK) voltage equation is used to calculate the reversal potential in such circumstances. Using Na^{+}, K^{+} and Cl^{-} as an example,

$$E_{\text{rev}} = \frac{RT}{F} \ln \left(\frac{P_{\text{Na}}[\text{Na}^{+}]_{\text{o}} + P_{\text{K}}[\text{K}^{+}]_{\text{o}} + P_{\text{Cl}}[\text{Cl}^{-}]_{\text{i}}}{P_{\text{Na}}[\text{Na}^{+}]_{\text{i}} + P_{\text{K}}[\text{K}^{+}]_{\text{i}} + P_{\text{Cl}}[\text{Cl}^{-}]_{\text{o}}} \right) , \tag{2}$$

where P_{B} is the permeability of the channel to ion B. The GHK equation can also be used to calculate the resting potential of the membrane and the

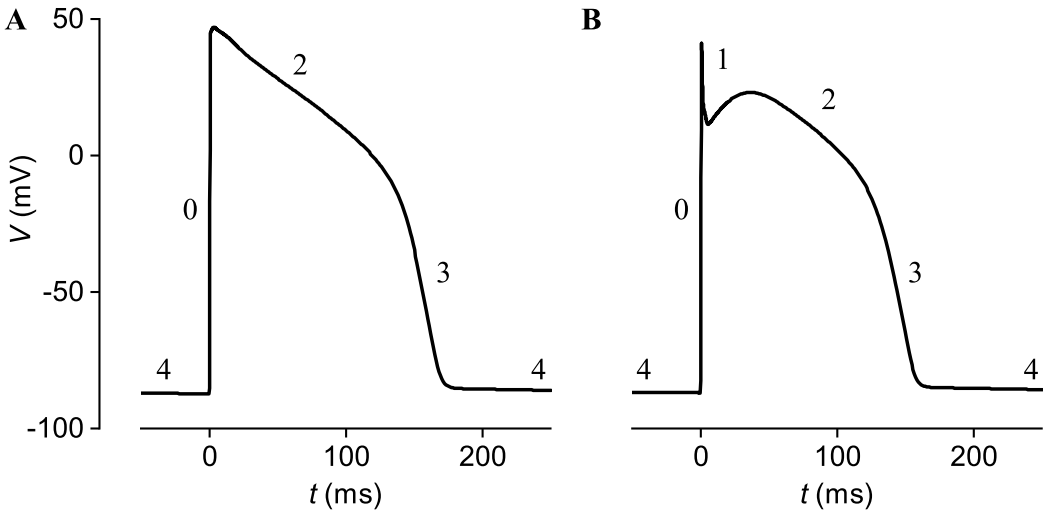

Figure 1: Phases of the action potential in endocardial (left) and epicardial (right) myocytes. The epicardial action potential shows a characteristic spike-and-dome morphology, which is attenuated in endocardial cells. The midmyocardial action potential morphology is similar to that in epicardial cells, but with a longer action potential duration (∼7–31% longer in non-failing human tissue [26]). Action potentials shown here were simulated using the Luo-Rudy model [27] at a basic cycle length of 500 ms.

direction in which the membrane potential will move if the permeabilities of ionic species are altered (e.g. through ion channel gating). From the GHK equation we can see that the membrane potential will tend to move towards the equilibrium potential of the ionic species whose permeability is the greatest, as the equilibrium potential of that ion will dominate E_{rev}. For example, when a cardiac myocyte is at rest, $P_{\text{K}} \gg P_{\text{Na}}$ and so the membrane potential V moves towards (although not all the way to) E_{K}, which is approximately -90 mV and near the resting membrane potential. When the cell is depolarised past threshold, $P_{\text{Na}} \gg P_{\text{K}}$ and so V moves from its resting value towards E_{Na}, which is at a positive potential of approximately 80 mV and so results in phase 0 depolarisation and an action potential.

2.2. The Ventricular Action Potential

The ventricular action potential is a transient change in the potential across a cell membrane (see Fig. 1) that propagates throughout the ventricles to trigger contraction of the ventricular muscle. The ventricular action potential can be broken down into distinct phases, each of which is associated

with specific ionic currents which differ not only in different regions of the heart but in different regions of the ventricular tissue. Phase 0, the upstroke, is the initial rapid depolarisation of the membrane to a positive potential. In epicardial and midmyocardial cells, there is then a rapid phase 1 repolarisation that is absent in endocardial cells. A plateau in the membrane potential (phase 2) then occurs before a final stage of repolarisation (phase 3). Phase 4 is the resting membrane potential. The presence of phase 1 repolarisation in epicardial and midmyocardial gives rise to the characteristic spike and dome morphology of action potentials recorded from these cells. The action potential is an all-or-none event, such that a perturbation to the membrane potential that takes it from its resting level past a threshold will result in phase 0 depolarisation. This all-or-none response is characteristic of a wide range of physical, chemical and biological systems, including nerve and muscle, and is termed *excitability*. The action potential is determined by a complex interplay between several ionic membrane currents, pumps and exchangers, with different directions (i.e. inwards or outwards), magnitudes and kinetics that determine their time course and effect on the action potential morphology (see Fig. 2). Here, a brief overview of the principal ionic currents found in ventricular myocytes, and their relation to the phases of the action potential, is given; a detailed review can be found in [28].

Sodium currents: There are two principal Na^+ currents in ventricular myocytes. As the Na^+ concentration is greatest outside the cell and the reversal potential of the currents is greater than maximum membrane potential, the Na^+ currents are always inward, at least under physiological conditions. The major Na^+ current is the fast inward current, I_{Na}, which is responsible for the rapid phase 0 upstroke of the action potential. I_{Na} has a relatively large amplitude and is both voltage- and time-dependent. It is controlled by three processes – an activation gate and two inactivation gates, one of which has rapid kinetics and one having slower kinetics. The kinetics of the activation and fast inactivation gates result in I_{Na} activating and inactivating in only a few milliseconds. The slow inactivation gate is responsible for the channel's slow recovery from inactivation. At resting membrane potential I_{Na} is zero, but activates when the membrane potential is raised to approximately -60 mV by current flowing from neighbouring cells when *in vivo* or by a stimulus current in isolated cells. The second Na^+ current is the late Na^+ current, $I_{Na,L}$. This current has a smaller amplitude than I_{Na} but the inactivation kinetics are slower, having a time constant of around 600 ms [30]. $I_{Na,L}$ has been shown to be partly responsible for the different action potential wave-

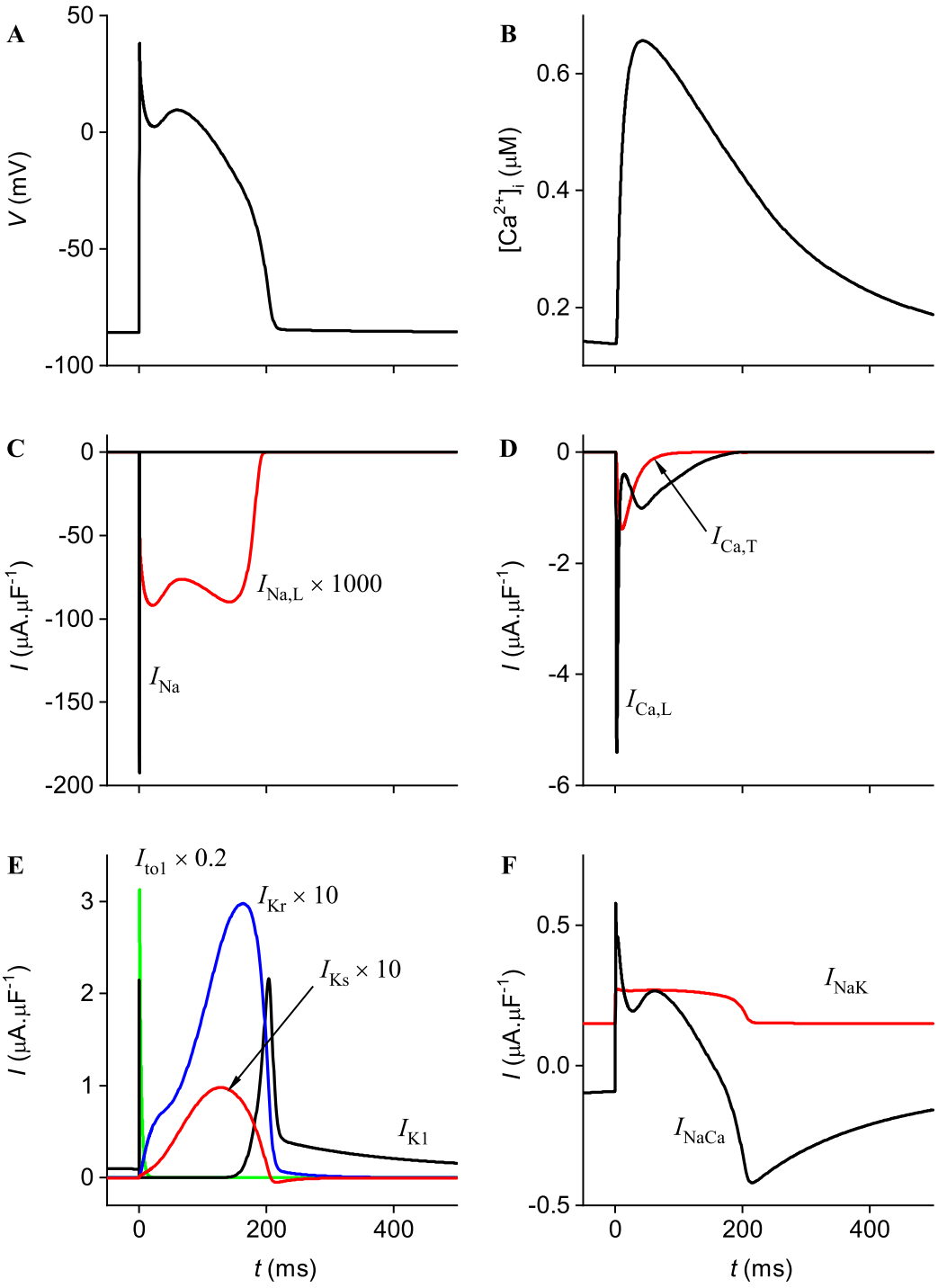

Figure 2: The action potential (A), intracellular calcium transient (B), and time course of the principal membrane currents in the ventricular myocyte: (C) Na^+ currents, note the rescaling of $I_{Na,L}$; (D) Ca^+ currents; (E) K^+ currents, note the rescaling; (F) pump and exchanger currents. See text for details. All were simulated at a basic cycle length of 800 ms using the Hund-Rudy epicardial model [29] with the exception of $I_{Ca,T}$, which is from the Luo-Rudy model [27] and was scaled to match the Hund-Rudy model action potential duration

form in epicardial, midmyocardial and endocardial regions of the ventricle [31].

Calcium currents: There are two types of Ca^{2+} channels in ventricular myocytes; L-type (the L indicating a "long-lasting" current with a "large conductance") and T-type (the T indicating "transient opening" and "tiny conductance"). Both channels have a high selectivity for Ca^{2+} and, as Ca^{2+} is at a higher concentration outside compared to inside the cell and the reversal potential is more positive than the maximum membrane potential, both are inward currents. The current through the L-type channels, $I_{\mathrm{Ca,L}}$, is larger than that through the T-type channels, $I_{\mathrm{Ca,T}}$, and the two currents have different voltage dependencies and kinetics: $I_{\mathrm{Ca,L}}$ activates at around -40 mV while $I_{\mathrm{Ca,T}}$ activates at more negative potentials, e.g. approximately -60 mV [32, 33]. $I_{\mathrm{Ca,L}}$ is both voltage- and time-dependent, and also has Ca^{2+}-dependent inactivation and so inactivates in response to a rise in Ca^{2+} on the intracellular side of the channel. The flow of Ca^{2+} ions through the channel causes a large release of Ca^{2+} from the sarcoplasmic reticulum (SR), a large intracellular Ca^{2+} store. This process is known as Ca^{2+}-induced Ca^{2+} release (CICR) and is responsible for the rise of intracellular Ca^{2+} (the Ca^{2+} transient) and the consequent tension development in the cell. This is the process of excitation-contraction coupling [1–3]. $I_{\mathrm{Ca,L}}$ is also responsible for maintaining the membrane potential plateau during phase 2 of the action potential. The physiological role of $I_{\mathrm{Ca,T}}$ in ventricular myocytes is less clear, although in the sino-atrial and atrioventricular nodes of the heart it is partly responsible for pacemaker activity [34].

Potassium currents: K^+ currents show the most electrophysiological variation of the major ionic currents in the heart, in that there are many different types of K^+ currents carried by different channels; here only the major K^+ currents will be considered. K^+ concentration is greatest inside the cell and the reversal potential is negative compared to resting membrane potential, and so K^+ currents are outward currents under physiological conditions. I_{K1} is the time-independent or inward rectifier current, and in ventricular myocytes is responsible for maintaining the resting membrane potential. I_{K1} shows little time dependence and is active over a wide range of membrane potentials. The current reverses at $E_{\mathrm{K}} \approx -90$ mV. At membrane potentials negative to this the current is inward, although under physiological conditions the membrane potential never drops below this value. The outward currents at membrane potentials positive to -90 mV show inward rectification. The transient outward K^+ current, I_{to1}, is responsible for phase 1

repolarisation and the spike and dome morphology seen in epicardial and midmyocardial ventricular myocytes [35]. The current is not seen at any significant magnitude in endocardial cells (e.g. [36]) and so this current, along with I_{Ks} (see below) and to a lesser extent several other currents, is responsible for transmural heterogeneities in electrophysiology. The delayed rectifier current is composed of two major parts – a rapid component, I_{Kr}, and a slow component, I_{Ks} [37]. The relative densities of the two currents vary between species. In guinea pig for example, I_{Ks} is larger [37] while in canine, I_{Kr} is the largest [38]. The currents oppose the depolarisation drive of $I_{\mathrm{Ca,L}}$ (that maintains the action potential plateau) and are therefore responsible for phase 3 repolarisation; as such, they have a significant influence on action potential duration. Loss-of-function mutations to KvLQT1, MinK and HERG genes cause down-regulation of I_{Ks} and I_{Kr}, leading to long QT syndromes 1 and 2 [39]. Along with I_{to1}, I_{Ks} is a major determinant of transmural heterogeneities of electrophysiology.

Pumps and exchangers: The flow of ions through Na^+, Ca^{2+} and K^+ channels causes dynamic changes in the intra- and extracellular concentrations of these ions. These changes are counteracted by the actions of the Na^+-K^+ ATPase and the Na^+-Ca^{2+} exchanger, both of which are electrogenic and therefore contribute to the action potential. The Na^+-K^+ ATPase hydrolyses adenosine triphosphate (ATP) to produce energy and pump Na^+ and K^+ up their concentration gradients. Three Na^+ ions are carried out of the cell for every two K^+ ions brought in, and so the net flux of ions results in the Na^+-K^+ ATPase current, I_{NaK}, being outward. The Na^+-Ca^{2+} exchanger can operate in forward or reverse modes. In forward mode (sometimes referred to as "normal mode") the exchanger uses the Na^+ concentration gradient to move three Na^+ ions into the cell, and one Ca^{2+} ion is extruded. The exchanger is therefore electrogenic and in forward mode the exchanger current, I_{NaCa}, is depolarising. However, the protein can be reversed depending on the Na^+ and Ca^{2+} concentrations and on the membrane potential. At resting concentrations, the reversal potential of the current is between -40 and -20 mV and, as membrane potential is around -80 mV, the exchanger operates in forward mode and an inward current is produced. During the fast upstroke of phase 0 depolarisation, membrane potential becomes more positive than the reversal potential and the current reverses, extruding three Na^+ ions for every Ca^{2+} ion brought in. During the plateau phase of the action potential, intracellular Ca^{2+} concentration rises (the Ca^{2+} transient) and the reversal potential of I_{NaCa} also changes, approximately following the

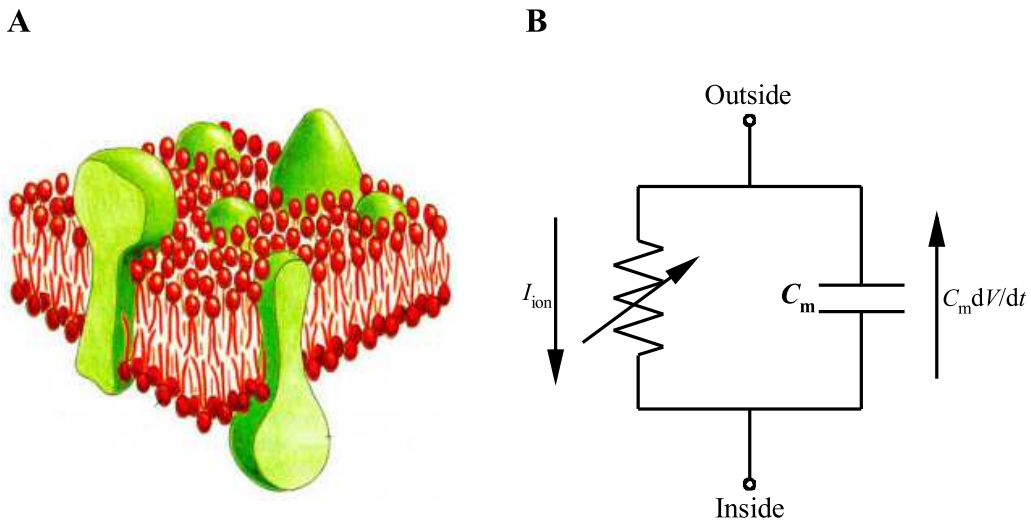

Figure 3: (A) Schematic diagram of the cell membrane, showing the lipid bilayer and transmembrane proteins (e.g. ion channels, pumps, exchangers). Modified from [40]. (B) Electrical circuit model of the cell membrane, with the variable resistor representing ion channels, pumps and exchangers, and the capacitor representing the lipid bilayer

Ca^{2+} transient. The reversal potential then is more positive than membrane potential and I_{NaCa} again operates in forward mode to extrude Ca^{2+} brought into the cell. I_{NaCa} therefore changes direction during the course of an action potential.

2.3. The Cell Membrane as an Electrical Circuit

The cell membrane is organised as a phospholipid bilayer, arranged so that the hydrophobic tails of the lipids lie together in the middle of the membrane while the hydrophilic heads form the outside of the membrane and are in contact with the aqueous solution of the intra- and extracellular spaces. Proteins (e.g. ion channels, pumps and exchangers) span this lipid bilayer to allow the passage of ions (Fig. 3A). As the membrane is an insulating material separating regions of charge (i.e. the intra- and extracellular spaces) then it can be thought of as a capacitor, with the ion channels, pumps and exchangers through the membrane thought of as variable resistors. The membrane can therefore be modelled as an electrical circuit with a capacitor (the lipid bilayer) and a variable resistor (the ion channels) in parallel (Fig. 3B). Current can flow through the circuit either through the resistor

(the ionic current) or by charging the membrane capacitance (the capacitive current). The charge across the capacitor, Q, is the product of capacitance and the voltage necessary to hold the charge:

$$Q = C_{\mathrm{m}} V \ . \tag{3}$$

Since the capacitive current in Fig. 3B is $\mathrm{d}Q/\mathrm{d}t$ (current is charge per unit time) and the magnitude of the capacitor, C_{m}, is constant (at 1 μF.cm^{-2} for a cardiac cell membrane), then if equation (3) is differentiated with respect to time such that

$$\frac{\mathrm{d}Q}{\mathrm{d}t} = C_{\mathrm{m}} \frac{\mathrm{d}V}{\mathrm{d}t} \ , \tag{4}$$

it can be seen that the capacitive current $\mathrm{d}Q/\mathrm{d}t$ can also be expressed as $C_{\mathrm{m}}\mathrm{d}V/\mathrm{d}t$. Since the flow of charge between the inside and outside of the membrane must be conserved, then from Kirchhoff's current law the sum of the capacitive and ionic currents in Fig. 3B must be zero:

$$C_{\mathrm{m}} \frac{\mathrm{d}V}{\mathrm{d}t} + I_{\mathrm{ion}} = 0 \ , \tag{5}$$

or more commonly

$$C_{\mathrm{m}} \frac{\mathrm{d}V}{\mathrm{d}t} = -I_{\mathrm{ion}} \ . \tag{6}$$

Therefore, the rate of change of the membrane potential, $\mathrm{d}V/\mathrm{d}t$, is determined by the sum of the ionic currents, I_{ion}. We can model an ionic current I_i with a linear instantaneous current-voltage relationship as

$$I_i = g_i(V - E_{\mathrm{rev}}) \ , \tag{7}$$

where g_i is the channel conductance and $V - E_{\mathrm{rev}}$ is the electrochemical gradient. In order to model an action potential – a transient change in membrane potential – using equations (6) and (7), a suitable form for I_{ion} and the conductances g_i must be determined. This was first described quantitatively for the squid giant axon by Hodgkin and Huxley in 1952.

2.4. Hodgkin-Huxley Formalism

In a series of five papers published in the *Journal of Physiology* in 1952 [41–45], Alan Hodgkin and Andrew Huxley, along with Bernard Katz who was a co-author on the first paper and a collaborator in several related studies, determined the dynamics of the ionic conductances that determine the

action potential in the squid giant axon. They utilised the experimental procedures of space clamping (inserting a thin metallic conductor along the length of the axon in order to provide low axial resistance and remove any spatial gradients in membrane potential) and voltage clamping (applying a feedback current to the cell in order to keep the membrane potential at a specified value, the command potential), both recently developed by Kenneth Cole and George Marmont with colleagues. (For a history and review of the experimental and mathematical background to the Hodgkin-Huxley model, see [46, 47].) Here, the method of describing channel gating using Hodgkin-Huxley formalism will be described. This formalism is still used in the current generation of biophysically detailed models, yet it is perhaps best to describe it in the context of the original Hodgkin-Huxley model.

It has already been shown that a cell membrane may be modelled as a capacitor in parallel with an ionic current (equation 6). Hodgkin and Huxley identified that, in the squid giant axon, the principal ionic currents are the Na^+ and K^+ currents, and that the other smaller currents, composed mainly of the Cl^- current, could be lumped together into a single "leakage" current. Therefore, equation (6) can be re-written for the Hodgkin-Huxley model as

$$C_{\mathrm{m}}\frac{\mathrm{d}V}{\mathrm{d}t} = -I_{\mathrm{Na}} - I_{\mathrm{K}} - I_{\mathrm{L}} - I_{\mathrm{stim}} \ , \tag{8}$$

where I_{Na} is the sodium current, I_{K} is the potassium current, I_{L} is the leakage current and I_{stim} is any applied stimulus current. Furthermore, since the single channel instantaneous I-V curves for open Na^+ and K^+ channels in the squid giant axon are approximately linear, each current can be written as the product of a conductance, g, and a driving force $V - E_{\mathrm{rev}}$ as in equation (7), where E_{rev} is the reversal potential of the current which is given by the Nernst equation (1). Note that by using the equilibrium potentials for the respective channel reversal potentials, it is assumed that the channels are selective for only one ionic species. It was also assumed that g_{L} was constant, such that $g_{\mathrm{L}} = \bar{g}_{\mathrm{L}}$, where $\bar{g}_{\mathrm{L}}$ is the maximal leakage current conductance. Equation (8) can therefore be written as

$$C_{\mathrm{m}}\frac{\mathrm{d}V}{\mathrm{d}t} = -g_{\mathrm{Na}}(V - E_{\mathrm{Na}}) - g_{\mathrm{K}}(V - E_{\mathrm{K}}) - \bar{g}_{\mathrm{L}}(V - E_{\mathrm{L}}) - I_{\mathrm{stim}} \ . \tag{9}$$

As the influx of Na^+ and the efflux of K^+ were found to be small during an action potential (3.7 and 4.3 pmoles.cm^{-2}, respectively), it was assumed that

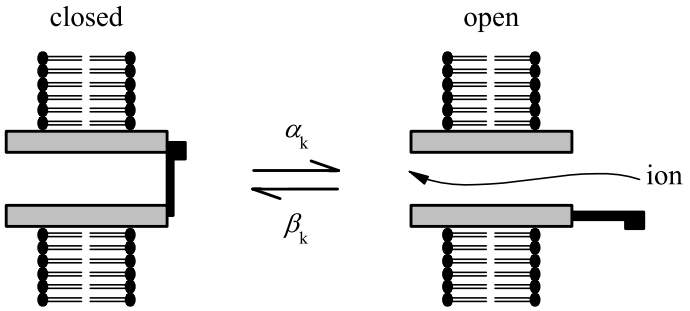

Figure 4: Schematic diagram of a simple gating scheme. The channel oscillates between open and closed states with the rate constants α and β. This gating scheme is not representative of actual channel structure and function, yet it is a useful model that allows the mathematical reconstruction of gating kinetics

all ionic concentrations were constant. As such, the equilibrium potentials are also constant.

In order to solve equation (9) it is necessary to determine the conductances g_{Na} and g_{K}, which vary with membrane potential and time. For a unit area of membrane (1 cm^2 in the case of the Hodgkin-Huxley model), any conductance g can be given as the product of the single channel conductance, γ, the number of channels per unit area of membrane, N, and the open probability of a single channel, P_{open} where $0 \leq P_{\mathrm{open}} \leq 1$, which is the same as the fraction of the channels in the open state. Therefore

$$g = \gamma N P_{\mathrm{open}} \ . \tag{10}$$

The maximal conductance per unit area of membrane, $\bar{g}$, is determined by γ and N, which are constants:

$$\bar{g} = \gamma N \ , \tag{11}$$

and so equation (10) can be written as

$$g = \bar{g} P_{\mathrm{open}} \ . \tag{12}$$

The conductances are therefore the product of a maximal conductance, $\bar{g}$, which is a constant, and the probability of a channel being in the open state, P_{open}, which is determined by gating variables.

Suppose a simple channel is assumed to be controlled by a single charged gate (i.e. the gate is voltage-dependent) that can be in either a closed or an

open state (see Fig. 4) that moves between the two states with an opening rate constant α and a closing rate constant β:

$$\text{Closed} \underset{\beta(V)}{\overset{\alpha(V)}{\rightleftharpoons}} \text{Open} \ .$$

(Note that channels can be controlled by more than one gating process, as described later, but here it is simpler and more intuitive to assume a single gating process. Note also that the gating mechanism is not necessarily voltage-dependent, but could be mediated by chemical signals such as ionic concentrations, as for L-type calcium current inactivation, or by mechanical stimuli, as with stretch-activated channels.) The probability that the channel will be open, P_{open}, is the same as the fraction of the total N channels in the open position, k, and so we can say $P_{\text{open}} = k$. If all of the N channels are open, $k = 1$, if all the channels are closed, $k = 0$. If k is the fraction of channels in the open state, then because the number of channels is constant, $1 - k$ is the fraction of channels in the closed state, and the rates of opening and closing are therefore

$$\text{Rate of opening} = \alpha_k(1 - k) \ , \tag{13}$$

$$\text{Rate of closing} = \beta_k k \ . \tag{14}$$

The net rate of change of the fraction of channels in the open state is the difference between these rates of opening and closing, and so

$$\frac{\mathrm{d}k}{\mathrm{d}t} = \alpha_k(1 - k) - \beta_k k \ . \tag{15}$$

It is this differential equation that is used to describe a gating mechanism. To see how the equation works, suppose that the membrane potential is at some voltage V_0 and the gating variable k is at a steady-state value k_0 appropriate to this voltage. The rate coefficients α_k and β_k also have values appropriate to the voltage V_0. If V_0 is stepped to a new voltage then α_k and β_k instantaneously take on the new values appropriate to this new voltage and the differential equation (15) determines how k_0 approaches its new value k_∞. The solution to the differential equation (15) is

$$k = k_\infty - (k_\infty - k_0)\exp(-t/\tau_k) \ , \tag{16}$$

where

$$k_\infty = \frac{\alpha_k}{\alpha_k + \beta_k} \ , \tag{17}$$

and

$$\tau_k = \frac{1}{\alpha_k + \beta_k} \ , \tag{18}$$

where τ_k is a voltage-dependent time constant. The steady-state function for k, equation (17), can be derived by substituting $\mathrm{d}k/\mathrm{d}t = 0$ and $k_\infty = k$ into equation (15) and rearranging with respect to k_∞. The time constant τ_k is the reciprocal of the sum of the rate coefficients. Equation (16) shows that, upon stepping to a new voltage, k will change from its old value k_0 and approach its new value k_∞ with an exponential time course. The rate coefficients α_k and β_k determine how quickly k approaches its new value: if the sum of α_k and β_k is large then τ_k will be small and the rate of change will be fast, and *vice versa*.

However, it is still necessary to experimentally determine the voltage-dependent rate coefficients α_k and β_k. To do this, an experimental voltage-clamp protocol is utilised such that values of α_k and β_k can be determined at specific voltages. From macroscopic current traces when V is clamped to a new voltage, k_∞ and τ_k can be determined and α_k and β_k for the specific clamped voltage are calculated as solutions to

$$\alpha_k = \frac{k_\infty}{\tau_k} \ , \tag{19}$$

$$\beta_k = \frac{1 - k_\infty}{\tau_k} \ , \tag{20}$$

which are derived from equations (17) and (18). Values of α_k and β_k can then be plotted as functions of the membrane potential at which they were recorded, and an equation fitted to these data in order to obtain continuous functions of α_k and β_k. It is this protocol that Hodgkin and Huxley utilised when determining the time course of the conductances g_{Na} and g_{K} during an action potential, and which will now be described.

For the Hodgkin-Huxley model, it is perhaps easier to start with the K^+ conductance g_{K}, as only a single process is involved. Figures 5A and B show experimental voltage clamp recordings (open circles) of the K^+ conductance from [45]. In Fig. 5A, the membrane is depolarised and the conductance g_{K} follows a sigmoidal increase to its new value. Upon depolarisation, g_{K} follows an exponential decrease to its original value. Hodgkin and Huxley modelled this conductance by raising a single gating process as described above to the fourth power, such that

$$g_{\mathrm{K}} = \bar{g}_{\mathrm{K}} n^4 \ , \tag{21}$$

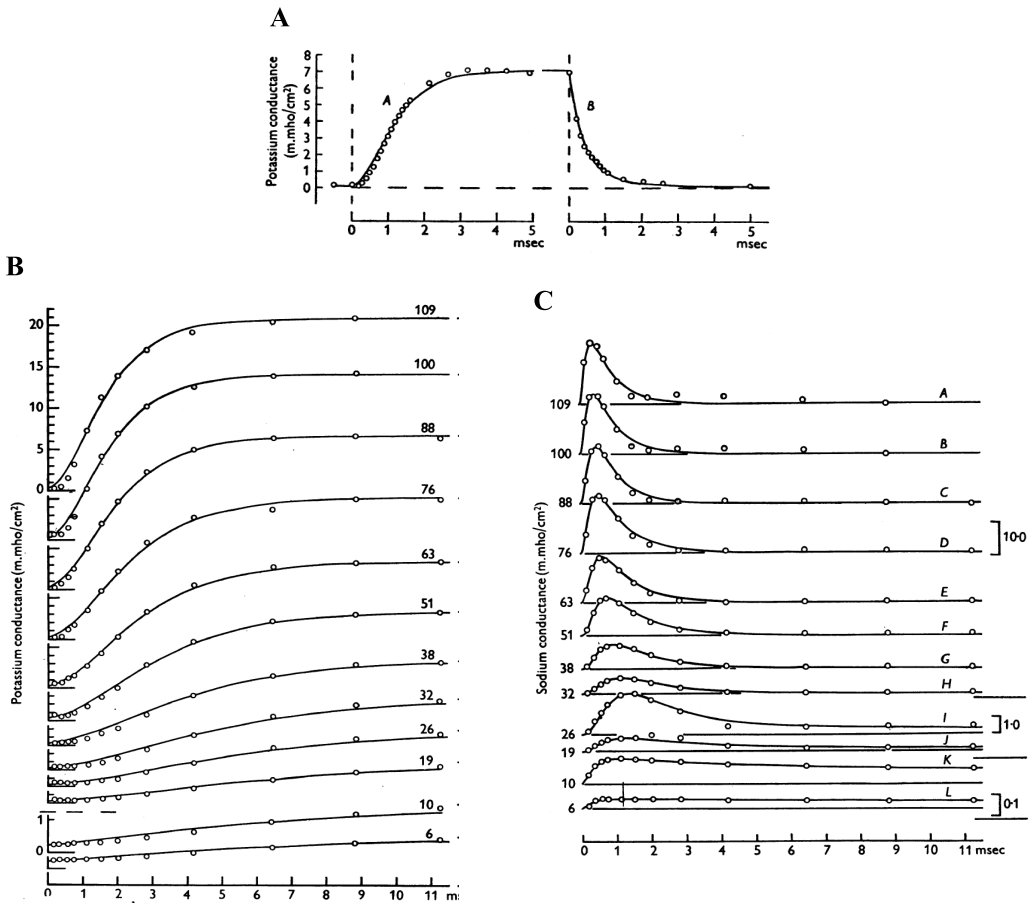

Figure 5: Experimentally recorded conductance changes in squid giant axon (open circles) and solutions to the Hodgkin-Huxley equations (smooth curves), as functions of time. (A) Response of K^+ conductance to a step increase in membrane potential, followed by a step decrease. (B) Responses of K^+ conductance to step increases in membrane potential of varying magnitudes. The ordinate scale is identical for curves A to J, but is increased fourfold for curves K and L for clarity. (C) Responses of Na^+ conductance to step increases in membrane potential of varying magnitudes. Ordinate scale bars are shown on the right. Each trace in panel B and C is labelled with the magnitude of the step voltage v from resting membrane potential in mV (i.e. $V = V_{\text{rest}} + v$). From [45].

where $\bar{g}_{\mathrm{K}}$ is the maximal K^+ conductance (which is also determined from the experimental recordings), and n is the fraction of K^+ channels in the open state (also known as the K^+ channel gating variable). This equation is analogous to equation (12) described earlier. Raising n to the fourth power was not chosen for any physiological reason, but simply because it gave the best fit to the experimental data. The differential equation describing the rate of change of n is therefore

$$\frac{\mathrm{d}n}{\mathrm{d}t} = \alpha_n(1-n) - \beta_n n \ . \tag{22}$$

As described before, the solution to this equation is

$$n = n_\infty - (n_\infty - n_0)\exp(-t/\tau_n) \ , \tag{23}$$

with the steady-state value of n given as

$$n_\infty = \frac{\alpha_n}{\alpha_n + \beta_n} \ , \tag{24}$$

and the time constant as

$$\tau_n = \frac{1}{\alpha_n + \beta_k} \ . \tag{25}$$

To construct continuous functions of α_n and β_n, values for n_∞ and τ_n were determined at specific voltages from the experimental results shown in Fig. 5B, utilising a form of equation (23) along with equation (21) that was suitable for fitting to the experimental recordings, namely

$$g_{\mathrm{K}} = \left\{(g_{\mathrm{K}\infty})^{1/4} - \left[(g_{\mathrm{K}\infty})^{1/4} - (g_{\mathrm{K}0})^{1/4}\right]\exp(-t/\tau_n)\right\}^4 \ , \tag{26}$$

with $g_{\mathrm{K}0}$ the initial conductance at $t = 0$, and $g_{\mathrm{K}\infty}$ the conductance at the end of the voltage pulse. The value for n_∞ at a particular voltage was then given by $g_{\mathrm{K}\infty}$, as a fraction of the maximal $g_{\mathrm{K}\infty}$ attained during all the voltage clamp experiments, with τ_n for a particular voltage chosen to give the best fit to the experimental data. (Although Hodgkin and Huxley fitted curves to data showing the time course of the K^+ conductance in order to obtain values of n_∞ and τ_n, the same results can be obtained from macroscopic current traces without isolating the conductance; see reference [48].) α_n and β_n were then calculated at each voltage using equations (19) and (20), these

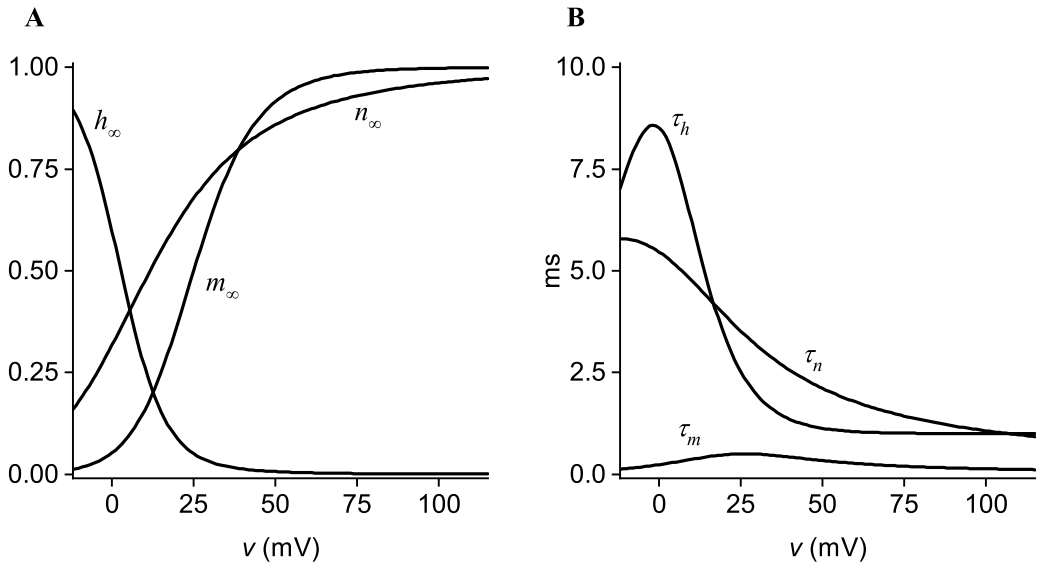

Figure 6: Steady state values (A) and time constants (B) of the Hodgkin-Huxley gating variables as functions of v. Gates m and h are the Na^+ channel activation and inactivation gates, respectively. Gate n is the K^+ channel gate

were plotted against voltage, and best fit functions were determined. These functions, which are voltage-dependent, are

$$\alpha_n = 0.01 \frac{10 - v}{\exp\left(\frac{10-v}{10}\right) - 1} \ , \tag{27}$$

$$\beta_n = 0.125 \exp\left(\frac{-v}{80}\right) \ , \tag{28}$$

where v is the deviation of the membrane potential V from rest ($V = V_{\text{rest}} + v$) in mV. It is these α_n and β_n rate coefficients that are used to calculate the voltage-dependent steady-state gating values [n_∞; equation (24] and time constants [τ_n; equation (25)] for the K^+ channel, as shown in Fig. 6.

Examining the time course of the experimentally recorded Na^+ conductance in Fig. 5C (open circles), it is apparent that two processes are working. The first is responsible for the increase in conductance, the second causing the conductance to decrease. Thus, during a voltage clamp to a new membrane potential, the current first activates and then inactivates, all at the

same membrane potential. To model this, Hodgkin and Huxley proposed that the Na^+ conductance takes the form

$$g_{\mathrm{Na}} = \bar{g}_{\mathrm{Na}} m^3 h \ , \tag{29}$$

where $\bar{g}_{\mathrm{Na}}$ is the maximal Na^+ conductance, m is the Na^+ activation gating variable, and h the Na^+ inactivation gating variable. Both gating variables are modelled using the differential equation (15), as for the K^+ current gating variable n, and functions for α_m, β_m, α_h and β_h determined in a similar way to that described for the K^+ conductance:

$$\alpha_m = 0.1 \frac{25 - v}{\exp\left(\frac{25-v}{10}\right) - 1} \ , \tag{30}$$

$$\beta_m = 4 \exp\left(\frac{-v}{18}\right) \ , \tag{31}$$

$$\alpha_h = 0.07 \exp\left(\frac{-v}{20}\right) \ , \tag{32}$$

$$\beta_h = \frac{1}{\exp\left(\frac{30-v}{10}\right) + 1} \ , \tag{33}$$

The resultant Na^+ channel voltage-dependent steady-state activation and inactivation gating values (m_∞ and h_∞, respectively) and their associated time constants (τ_m and τ_m) are shown in Fig. 6.

The descriptions of the time- and voltage-dependence for both the Na^+ and K^+ conductances – equations (29) and (21) – can now be substituted into equation (9) to complete the model.

2.4.1. The Hodgkin-Huxley model of the action potential in the squid giant axon

In the previous section it was shown how Hodgkin and Huxley quantitatively described the dynamics of the gates m, h and n that determine the time course of V during an action potential. Here it will be shown how these dynamics interact to result in the action potential. Note that Hodgkin and Huxley used the term v to denote the deviation of V from its resting level, where negative v denotes depolarisation. In this section, $v = V - V_{\mathrm{rest}}$ will be used such that depolarisation is denoted by positive v, which is perhaps more intuitive as a depolarisation results in an increased membrane potential.

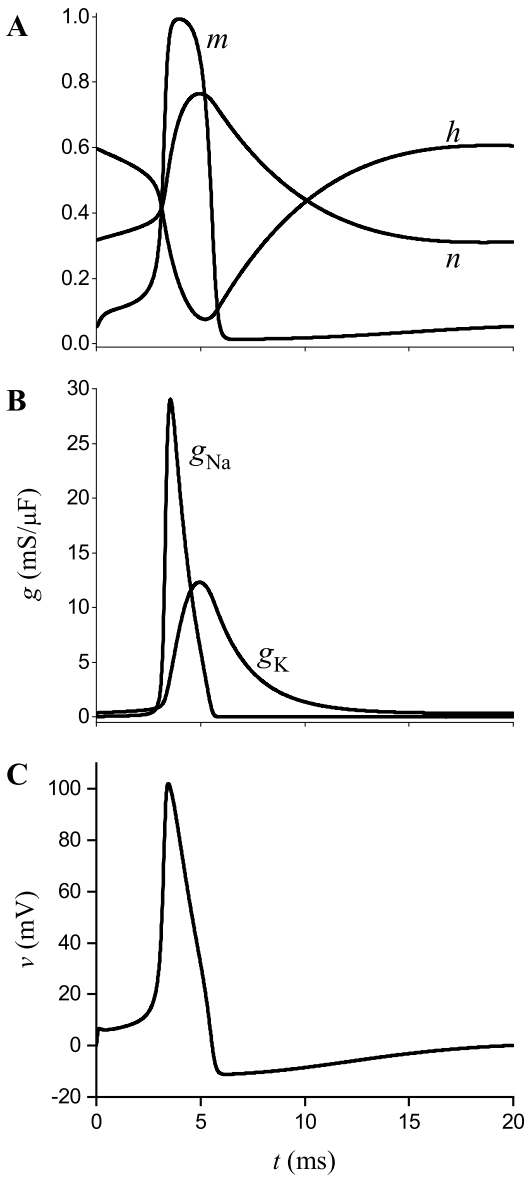

Figure 7: Time course of the Hodgkin-Huxley model gating variables (A) and conductances (B) underlying the action potential (C), in response to a 0.1 ms, -70 μA/μF stimulus current applied at $t = 0$ ms

When the cell is at rest ($v = 0$ mV) the K^+ conductance gating variables n^4 are dominant over the Na^+ conductance gating variables m^3h (see Fig. 6A) and so v tends towards the reversal potential for K^+, $v_K = -12$ mV. If a small current is applied to the cell, a small depolarisation occurs but v returns to the equilibrium resting value $v = 0$ mV. However, if the stimulus current is large enough to take v past a threshold then m, which is approaching m_∞ with a small time constant (see Fig. 6B) such that the process is fast, causes an increase in Na^+ conductance, an increase in the inward Na^+ current and a further, regenerative depolarisation. (For a qualitative phase space analysis of this threshold phenomenon, see reference [49].) Now the Na^+ conductance dominates over the K^+ conductance and v tends towards $v_{Na} = 115$ mV. The gates h and n have also been moving towards their new voltage-dependent values h_∞ and n_∞, although with much slower time constants (Fig. 6B). Eventually, however, h takes on its new, low value, the Na^+ conductance falls and the Na^+ current inactivates. At around the same time, K^+ activation is increasing as n approaches its new, high value. K^+ conductance then increases and becomes dominant, the K^+ current activates, and the membrane potential repolarises as v tends back towards v_K. There is then a refractory period during which further stimuli will not cause an increase in Na^+ conductance or, therefore, an action potential. This is due to the large time constant of the Na^+ inactivation gate h (i.e. a slow process), which causes a relatively long delay in h moving to its resting, open value at $v = 0$ mV. The time course of the gating variables m, h and n and the conductances g_{Na} and g_K are shown in Fig. 7A,B in response to a supra-threshold stimulus. These changing conductances result in the depolarisation and subsequent repolarisation of the membrane – the action potential, which is shown in Fig. 7C.

2.5. The FitzHugh-Nagumo Model

The FitzHugh-Nagumo (FHN) model [50–53] is a caricature of the four-variable Hodgkin-Huxley model that is still used, sometimes in modified form [54, 55], as a computationally tractable excitation model for studying propagation in cardiac tissue. The model has two variables, and can be related to the Hodgkin-Huxley model by assuming that m is an instantaneous function of v, while $h + n$ is constant at 0.8 (see Figs. 6A and 7A). Therefore m as a state variable can be removed by setting $m = m_\infty$, and h as a state variable can be removed by setting $h = 0.8 - n$. The two remaining state variables, v and n, then become excitation and recovery variables, respectively. The

qualitative features of the Hodgkin-Huxley model are kept if the excitation and recovery variables in the FHN model – which are termed v and w, respectively – have similar dynamics (see Fig. 8 and compare to Fig. 7C). The only constraints on choosing functions for the FHN equations are that the nullcline of v is cubic, the nullcline of w monotonically increases and, for an excitable system, the choice of parameter values results in a stable steady state where the nullclines cross (see [49] for a description of FHN model nullclines). One choice is

$$\frac{\mathrm{d}v}{\mathrm{d}t} = \frac{1}{\epsilon}\left(v - \frac{v^3}{3} - w\right) \ , \tag{34}$$

$$\frac{\mathrm{d}w}{\mathrm{d}t} = \epsilon(v + \beta - \gamma w) \ , \tag{35}$$

where the parameters $0 < \epsilon \ll 1$, $0 < \gamma$ and $|\beta| < \sqrt{3}$.

2.6. Markovian Formulations of Ion Channels

Markovian formulations for ion channels are used to model findings from molecular studies where an individual channel, away from its physiological cell environment, is found to exist in one of several specific states (e.g. closed, open, fast inactivated, slow inactivated). As such, Hodgkin-Huxley formalism, as represented by the simple schematic shown in Fig. 4, is unable to capture the more complicated dynamics exhibited by these channels. (Note that channels described by Hodgkin-Huxley formalism can be described using a simple Markovian formulation, but more complicated Markovian formulations cannot be represented using Hodgkin-Huxley formalism – see [56] for a detailed discussion.) Markovian formulations are particularly useful for modelling channelopathies due to genetic mutations or drug applications, where the ion channels are studied in isolated expression systems. A Markovian description of such experimental data combined with a cell or tissue model therefore enables the study of the effects of these single channel mutations on whole cell electrophysiology (e.g. [21, 57–62]).

For a general Markov gating model where each of N states can potentially change to any other state, the probability of occupying a particular state, P_i, at a given time t and voltage V can be given by a series of first-order linear differential equations:

$$\frac{\mathrm{d}P_i}{\mathrm{d}t} = -\sum_{j=1}^{N}[k_{ji} \cdot P_i(t,V)] + \sum_{j=1}^{N}[k_{ij} \cdot P_j(t,V)] \ , \tag{36}$$

$$\frac{\mathrm{d}P_N}{\mathrm{d}t} = -\sum_{j=1}^{N-1}\left[\frac{\mathrm{d}P_i}{\mathrm{d}t}\right] \ , \tag{37}$$

for $i = 1, 2...N-1$, $i \neq j$, and where k_{ij} is a voltage-dependent rate constant leading from state j to state i [63]. The rate constants, which are functions of membrane potential, are given by

$$k_{ij} = \exp(A_{ij} + B_{ij}V + C_{ij}V^2) \ , \tag{38}$$

where the parameters describe the potential energy barriers between the states: A_{ij} represents the energy barrier height in the absence of an electrical field, B_{ij} represents the energy barrier height that exists due to charge-field and dipole-field interactions and C_{ij} represents the contribution of total distortion polarisation or field induced dipoles [64]. In the limiting case of a low transmembrane field strength where the squared term is not required, equation (38) can be reduced to:

$$k_{ij} = \exp(A_{ij} + B_{ij}V) \ . \tag{39}$$

However, Matsuoka *et al.* [65] found that high membrane potentials produced large rate constants that interfered with integration of cellular equations. An alternative, four parameter format that included saturation of the rate constants was therefore proposed:

$$k_{ij} = \frac{1}{A_{ij}\exp(V/B_{ij}) + C_{ij}\exp(V/D_{ij})} \ . \tag{40}$$

Thus for a simple three-state chain Markov model of a single channel where C is a closed state, O an open state and I an inactivated state, the state diagram is

$$C \ \underset{k_{CO}}{\overset{k_{OC}}{\rightleftharpoons}} \ O \ \underset{k_{OI}}{\overset{k_{IO}}{\rightleftharpoons}} \ I \ ,$$

and from equations (36) and (37), the equations to this model are:

$$\frac{\mathrm{d}P_C}{\mathrm{d}t} = -k_{OC}P_C + k_{CO}P_O \ , \tag{41}$$

$$\frac{\mathrm{d}P_O}{\mathrm{d}t} = k_{OC}P_C - (k_{CO} + k_{IO})P_O + k_{OI}P_I \ , \tag{42}$$

$$\frac{\mathrm{d}P_I}{\mathrm{d}t} = -\frac{\mathrm{d}P_C}{\mathrm{d}t} - \frac{\mathrm{d}P_O}{\mathrm{d}t} \ . \tag{43}$$

Substituting equations (41) and (42) into equation (43) and simplifying gives:

$$\frac{\mathrm{d}P_I}{\mathrm{d}t} = -k_{OI}P_I + k_{IO}P_O \ . \tag{44}$$

In this situation there are four independent voltage-dependent rate constants (k_{CO}, k_{OC}, k_{OI} and k_{IO}) each having four parameters if equation (40) is used to define the rate constants, giving a total of 16 parameters (methods for obtaining these parameter values are discussed in [56, 66]). A typical equation for an ionic current will then take the form

$$I_{\mathrm{ion}} = \bar{g}P_O(V - E_{\mathrm{rev}}) \ , \tag{45}$$

so that the Hodgkin-Huxley-type gating variables are replaced with a single open probability, P_O, describing the conductance of the channel.

2.7. Development of Cardiac Cell Models

Although the Hodgkin-Huxley model provided a formalism for modelling the action potential and the FitzHugh-Nagumo model is useful for studying phenomena associated with propagation where the spatio-temporal behaviour of the wave of excitation is more important than the shape of the action potential, at a biophysical level they are models of neuronal action potentials and do not quantitatively reproduce the cardiac action potential due to their lack of ion channels specific to cardiac cells. Therefore a series of cardiac models have been developed to study problems specific to cardiac cells and tissue.

The development of the current generation of biophysically detailed ventricular cell models can be traced back to the Hodgkin-Huxley model, as it provided a formalism for modelling the action potential. The model of Noble [68, 69] for the Purkinje fibre was an adaptation of the Hodgkin-Huxley equations, and was the first biophysical model specifically for a cardiac cell. Cell models continued to be updated as the ionic basis of the cardiac action potential was determined experimentally. The discoveries of the cardiac Ca^{2+} current [70] and various components of what until then was considered as a single K^+ current [71, 72] were followed in the 1970s by the McAllister-Tsien-Noble model [73], again for the Purkinje fibre, and the first model of a

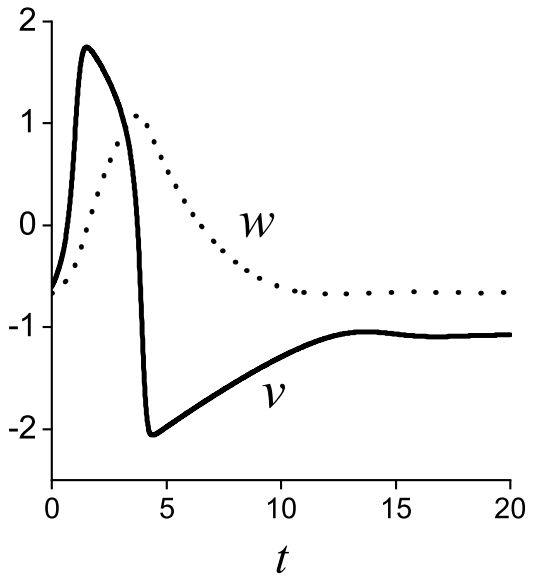

Figure 8: Time course of the FitzHugh-Nagumo excitation variable v (i.e. the action potential) and recovery variable w in response to a supra-threshold stimulus

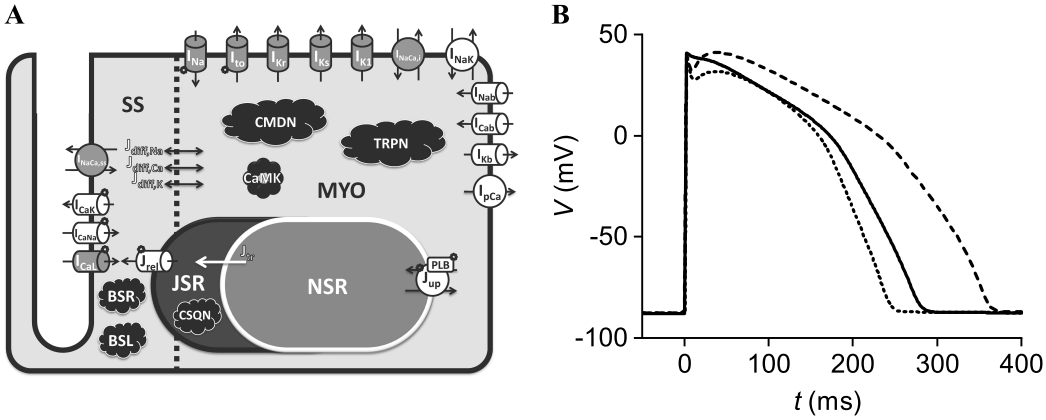

Figure 9: (A) Schematic of the O'Hara-Rudy human ventricular cell model, from [67]. (B) Periodic steady-state O'Hara-Rudy model action potentials at a basic cycle length of 1000 ms. Solid line, endocardial cell model; dashed line, midmyocardial cell model; dotted line, epicardial cell model. Note the morphological differences – especially the action potential duration – between these biophysically-detailed human cardiac cell models and the Hodgkin-Huxley model action potential in Fig. 7C

ventricular muscle cell, the Beeler-Reuter model [74]. The inclusion of ionic concentration changes along with the Na^+-K^+ ATPase and the Na^+-Ca^{2+} exchanger came with the publication of the DiFrancesco-Noble Purkinje fibre model [75], although the Ca^{2+} transient in the model was too large [10]. Accurate modelling of the intracellular calcium transient was the main focus of the Hilgemann-Noble model [76] that, while being a model for atrial cells, provided a basis for future models of ventricular calcium handling. In 1991 came the first phase of the Luo-Rudy model [77] followed in 1994 by the second phase incorporating dynamic concentration changes [27, 78]. The general outline of the Luo-Rudy model can be seen as a basis for many of today's biophysically detailed cell models which as a matter of course contain various membrane currents (including those activated only during pathological conditions), dynamic ion concentrations and various levels of Ca^{2+} handling, along with β-adrenergic control of E-C coupling (e.g. [79]) and different metabolic pathways (e.g. [80]). In recent years, data describing ionic currents and action potentials in human ventricular cells and tissues have become available, and this has allowed the development and validation of models describing human ventricular electrophysiology [67, 81–83] (see Fig. 9) that are perhaps more relevant than models of animal electrophysiology (especially rodents) in terms of clinical translatability.

The increased complexity in these models has been paralleled by an increase in computing power that allows large-scale temporal and spatial problems to remain tractable despite the increased levels of physiological detail; the current generation of biophysically detailed models typically include over 20 state variables for voltage, gating, ionic concentrations etc., each with a differential equation to solve, as well as numerous other variables modelled using upwards of 100 algebraic equations. A more detailed review of the development of biophysically detailed cardiac cell models highlighting the iterative interaction between modelling and experimentation is given in references [5, 10, 84].

2.8. Modelling Calcium Handling

Influx of Ca^{2+} through the L-type Ca^{2+} channels results in a large release of Ca^{2+} from the sarcoplasmic reticulum (an intracellular Ca^{2+} store), termed Ca^{2+}-induced Ca^{2+} release (CICR), and a transient rise of intracellular Ca^{2+} concentration (the "Ca^{2+} transient"). This Ca^{2+} transient not only causes contraction of the cell through binding of Ca^{2+} to troponin and the

subsequent interaction of actin and myosin filaments, but modulates membrane activity (e.g. *via* the Na^+-Ca^{2+} exchanger) and can, under certain conditions, be arrhythmogenic (e.g. [20]). Accurate modelling of intracellular Ca^{2+} handling is therefore necessary if an electrophysiology model is to be used to examine electrophysiological consequences of pathological conditions associated with Ca^{2+} overload and abnormal Ca^{2+} handling. A detailed description of modelling of Ca^{2+} handling in cardiac cells is presented in Part 1 of this two-part article (Colman et al., in this issue), while a historical examination of the interaction between experiment and modelling with regards to Ca^{2+} handling can be found in [85–88].

2.9. Methods of Integration

2.9.1. The forward Euler method

Although the ordinary differential equations used to describe the action potential in biophysically detailed excitation models are high order (i.e. many variables) and stiff (variables change with different time scales), they can be solved by simple finite difference methods. Typically, differential equations for membrane potential, e.g. those of the form of equation (6), and ionic concentrations are solved using a simple forward Euler method. If we represent such an equation by

$$\frac{\mathrm{d}x}{\mathrm{d}t} = f(x) \ , \tag{46}$$

then by integrating we wish to find the solution $x(t)$, subject to the condition that $x = x_0$ at time $t = t_0$. The forward Euler method assumes that over a sufficiently small time step Δt, the function $f(x)$ remains constant and so the change in x during the time step can be approximated by $f(x_0)\Delta t$. The new value of x at $t_0 + \Delta t$, which we shall call x_1, is therefore given as

$$x_1 = x_0 + f(x_0)\Delta t \ . \tag{47}$$

The variable x is now at x_1, the function $f(x_0)$ becomes $f(x_1)$, and t becomes $t_0 + \Delta t$. The next iteration will give us $x_2 = x_1 + f(x_1)\Delta t$ and take us to $t = t_1 + \Delta t$, and so on. The general scheme is given by

$$x_{n+1} = x_n + f(x_n)\Delta t \ , \tag{48}$$

and is the simplest possible method of numerical integration, although one that is prone to errors in the calculated solution if the time step Δt is not sufficiently small. For increased numerical accuracy, an integration scheme such as the fourth order Runge-Kutta method may be employed [89], although this will increase computation time with respect to the Euler method.

2.9.2. Integrating equations for gating variables

Integration of the equations describing gating variables with Hodgkin-Huxley formalism is carried out using the scheme of Rush and Larsen [90], who showed that the solution to the general gating equation

$$\frac{\mathrm{d}k}{\mathrm{d}t} = \alpha_k(V)(1-k) - \beta_k(V)k \ . \tag{49}$$

could be given by

$$k = k_\infty(V) - (k_\infty(V) - k_0)\exp(-\Delta t/\tau_k(V)) \ , \tag{50}$$

where Δt replaces t from the exact solution as in equation (16) if it was assumed that the α and β rate coefficients that define k_∞ and τ_k – equations (17) and (18) – remained constant over the sufficiently small time step Δt. For the subsequent iteration, k becomes k_0. This is known as the Rush-Larsen scheme, and is more accurate than integrating equation (49) with the forward Euler method as the solution to equation (50) is dependent only on the membrane potential V rather than the derivative of k.

2.9.3. Variable time steps

As the choice of Δt determines, to a large extent, the speed of integration, then it is desirable to have as large a time step as possible without reducing accuracy of the solutions, particularly during simulations with long pacing runs or when searching parameter space. When the solutions to the differential equations are changing slowly then a large time step may be used without compromising accuracy. As $\mathrm{d}V/\mathrm{d}t$ is the variable that changes most rapidly in the majority of models, a variable time step dependent on $\mathrm{d}V/\mathrm{d}t$ can be used such that Δt is large when $\mathrm{d}V/\mathrm{d}t$ is small, and *vice versa*. Thus, during the upstroke of the action potential, Δt will be small, but during the plateau and at resting membrane potentials, Δt can be large, allowing for faster integration. One relatively simple scheme for a variable time step that is used to integrate the Hund-Rudy equations describing canine ventricular electrophysiology [29] has the following conditions: if $\mathrm{d}V/\mathrm{d}t$ exceeds 1 mV/ms, up to 5 ms after $\mathrm{d}V/\mathrm{d}t$ exceeds this threshold, or within 2 ms before or after a stimulus current is applied, a minimum time step of $\Delta t = 0.005$ ms is used; between 5 and 20 ms after $\mathrm{d}V/\mathrm{d}t$ exceeds the 1 mV/ms threshold, a medium time step of $\Delta t = 0.01$ ms is used; at all other times a time step of $\Delta t = 0.1$ ms is used. Therefore, a small time step is used when the membrane

potential will be changing rapidly, i.e. phase 0 depolarisation, with larger time steps used at other times, and the time taken to integrate the equations is considerably reduced.

2.9.4. Tabulating exponential functions

One major computational demand is solving the exponential functions in the equations describing cell electrophysiology, as the program must call libraries of functions to solve the exponentials, a time-consuming process, especially with tissue-level simulations. As most of these exponential functions are explicitly voltage-dependent, it is possible to pre-calculate their values at certain voltages, and store these values in a lookup table that can be referred to by the program when needed. For cardiac excitation models, voltage-dependent exponential functions can be calculated for every voltage between -100 and $+100$ mV in 0.1 mV steps. Typically, there are around 40 such exponential equations in a cell model, and so a 40×2001 array is needed to store the pre-calculated function values. (Note that these lookup tables need to be expanded when simulating the effects of shocks on tissue, where voltage may go out of physiological ranges [91].) To further speed up computation time, the process could be extended to include other exponential or logarithmic functions such as reversal potentials and equations describing calcium handling.

3. Modelling Propagation in Ventricular Tissue

In an excitable medium such as cardiac tissue, cellular excitation propagates as waves of excitation. During normal sinus rhythm, the wave of excitation begins at the sinoatrial node, then propagates through the atria and the atrioventricular node, before moving down the His-Purkinje conducting system and exciting the endocardial surfaces of the ventricles. This is essentially a one-dimensional sequence, although propagation through the thin-walled atria may be considered as two-dimensional, and can be modelled as propagation in a two-dimensional sheet of tissue. The ventricles, however, are three-dimensional structures, with transmural and base-apical heterogeneities that affect both local excitation (e.g. membrane current densities and kinetics, and calcium handling) and the propagation of excitation (e.g. due to the influence of myocyte orientations and sheet structure), and so the modelling of propagation of excitation through the ventricles should be in three dimensions. However, one- and two-dimensional simulations can be

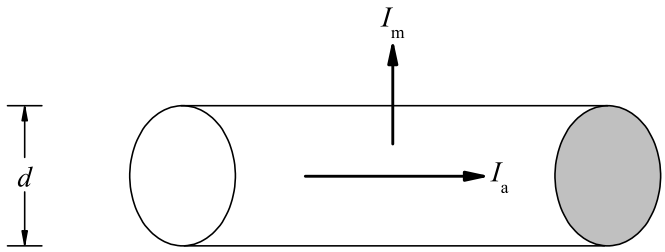

Figure 10: Schematic of a linear one-dimensional cable. I_m denotes the membrane current, I_a the axial current and d the diameter of the cable

useful for examining phenomena related to, for example, re-entrant arrhythmias, such as conduction velocity restitution (in 1D) and wavefront curvature (in 2D) [5].

If the coupling between cells is strong, as in the ventricles, then the ultrastructure of the tissue (cell membranes, connexins and gap junctions etc.) can be neglected and the tissue can be thought of as a continuous medium [92]. Such a continuous medium can be described using partial differential equations (PDEs), and so the tissue model in this case will be continuous state, continuous space and continuous time. Local membrane excitability in these PDE models can be described either by simple models such as the FitzHugh-Nagumo excitation equations [50–53] or their derivatives [54, 55] (see section 2.5), or by using biophysically detailed models such as those described in section 2.7. The propagation of excitation throughout the medium is then described using non-linear cable theory [93].

3.1. Propagation in One Dimension: Non-Linear Cable Theory

Propagation throughout ventricular tissue can be modelled using non-linear cable theory, extended from one spatial dimension to two or three as appropriate. Here, propagation along a simple cylindrical cable is considered – non-linear cable theory. Linear cable theory is discussed in detail in Jack *et al.* [93], with the non-linear excitation equations discussed earlier in Section 2 leading to a need to extend the theory to include non-linearities. Regardless of whether linear or non-linear, the derivation of the axial component of the cable equation is the same.

Figure 10 shows a schematic of a linear one-dimensional cable where the extracellular resistance is neglected such that the model is described as mon-

odomain. The membrane current I_{m} is modelled with capacitive and ionic components as described in Section 2. The intracellular fluid resistance is represented by an ohmic resistance so that, in the case where membrane conductance is zero and so no current flows across the membrane, the relation between intracellular voltage V and the axial current I_{a} can be be given by Ohm's law:

$$\frac{\Delta V}{\Delta x} = -r_{\mathrm{a}} I_{\mathrm{a}} \ , \tag{51}$$

where x is the distance along the cable, and r_{a} is the intracellular resistance to axial flow of current per unit length of cable, given by $R_{\mathrm{i}}/\pi d^2$ where R_{i} is the specific intracellular resistivity and d the diameter of the cable. Here it is assumed that the membrane conductance, and so the membrane current I_{m}, along the length Δx is zero. In the one-dimensional cable, larger values of V at smaller values of x (i.e. a negative $\Delta V/\Delta x$) should give rise to a positive axial current, i.e. the current flows down a potential gradient; the negative sign in equation (51) imposes this condition.

Membrane conductance, however, is rarely negligible, even at steady state due to the presence of leakage currents. It is therefore necessary to consider the differential form of equation (51) where Δx is given by the limit ∂x, and ∂V is the voltage difference:

$$\frac{\partial V}{\partial x} = -r_{\mathrm{a}} I_{\mathrm{a}} \ , \tag{52}$$

where $\partial V/\partial x$ and I_{a} are measured at the same point along the cable. As any change in the axial current I_{a} should come from flow of the membrane current I_{m}, then from Kirchhoff's current law the membrane current must be equal and opposite to the change in axial current across that point

$$\frac{\partial I_{\mathrm{a}}}{\partial x} = -I_{\mathrm{m}} \ . \tag{53}$$

If we assume that r_{a} remains constant along the length of the cable and differentiate equation (52) with respect to space to obtain

$$\frac{\partial^2 V}{\partial x^2} = -r_{\mathrm{a}} \frac{\partial I_{\mathrm{a}}}{\partial x} \ , \tag{54}$$

we can then substitute equation (53) into equation (54) to obtain

$$\frac{\partial^2 V}{\partial x^2} = r_{\mathrm{a}} I_{\mathrm{m}} \ , \tag{55}$$

and rearranging gives an equation for the membrane current

$$I_{\mathrm{m}} = \frac{1}{r_{\mathrm{a}}} \frac{\partial^2 V}{\partial x^2} \ . \tag{56}$$

It has already been shown in section 2.3 that I_{m} is composed of a capacitive and an ionic component such that

$$I_{\mathrm{m}} = C_{\mathrm{m}} \frac{\partial V}{\partial t} + I_{\mathrm{ion}} \ . \tag{57}$$

We now have two differential equations for the membrane current, one differentiated twice with respect to space, the other differentiated with respect to time. By combining these two equations, (56) and (57), we obtain the basic partial differential equation of non-linear cable theory:

$$\frac{1}{r_{\mathrm{a}}} \frac{\partial^2 V}{\partial x^2} = C_{\mathrm{m}} \frac{\partial V}{\partial t} + I_{\mathrm{ion}} \ . \tag{58}$$

As I_{ion} is related to V in a non-linear fashion, the equation cannot be solved analytically and so solutions must be obtained by numerical integration. Jack *et al.* [93] discuss the situation where I_{ion} has a linear relation with V and so can be solved analytically. By rearranging equation (58) and substituting in $D = 1/(C_{\mathrm{m}} r_{\mathrm{a}})$, where D is an *electrical diffusion coefficient* with units of $\mathrm{mm^2 ms^{-1}}$, to give

$$\frac{\partial V}{\partial t} = D \frac{\partial^2 V}{\partial x^2} - \frac{1}{C_{\mathrm{m}}} I_{\mathrm{ion}} \ , \tag{59}$$

we have a version of the non-linear cable equation which is a parabolic partial differential equation of the reaction-diffusion type, the component $(1/C_{\mathrm{m}})I_{\mathrm{ion}}$ being the membrane reaction and the component $D(\partial^2 V/\partial x^2)$ the diffusion of voltage along the cable. Equation (59) assumes that the diffusion coefficient D is constant throughout the medium. However, if D changes spatially, as is the case when fibre orientation is included in the model geometry or when including regions of ischaemic tissue, for example, we must take into consideration its spatial rate of change $\partial D/\partial x$, and so equation (59) becomes

$$\frac{\partial V}{\partial t} = \frac{\partial}{\partial x}\left(D \frac{\partial V}{\partial x} \right) - \frac{1}{C_{\mathrm{m}}} I_{\mathrm{ion}} \ . \tag{60}$$

It is sometimes more convenient to write equations (59) and (60) in the forms

$$\frac{\partial V}{\partial t} = D \Delta V - I_{\mathrm{ion}} \ , \tag{61}$$

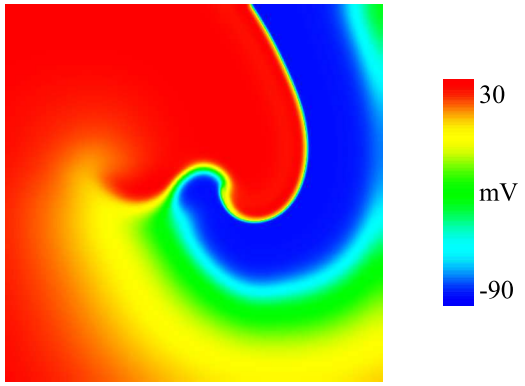

Figure 11: Re-entrant spiral wave solution in a 12 cm square homogeneous, isotropic two-dimensional virtual tissue, with excitation described using the epicardial ten Tusscher-Noble-Noble-Panfilov human ventricular model [81]

and

$$\frac{\partial V}{\partial t} = \nabla(D\nabla V) - I_{\text{ion}} \ , \tag{62}$$

respectively. Here $\Delta = \nabla^2 = \partial^2/\partial x^2$ is the Laplace operator, and $\nabla = \partial/\partial x$ is the spatial gradient operator, both in one spatial dimension for this example. The term $1/C_{\text{m}}$ is omitted here as $C_{\text{m}} = 1$ μF.cm^{-2} in most ventricular models.

3.2. Propagation in Two and Three Dimensions

Simulated propagation of excitation in two- and three-dimensional media allows a variety of wave phenomena to be studied, including, for example, re-entrant waves (e.g. [82]; see Fig. 11) and the effects of wavefront curvature [94]. The effects of myocyte orientations can be included in such models, an important consideration as propagation occurs faster along the myocyte than across it [95]. The equations used to model propagation in two- and three-dimensional media are extensions of the one-dimensional non-linear cable equation, extended to two and three dimensions and with the effects of myocyte orientation (and therefore anisotropy of diffusion) included.

There are three principal axes of diffusion throughout ventricular tissue – the myocyte direction (historically called the "fibre" direction), the sheet plane and the sheet normal [96]. Orthotropic propagation (i.e. different diffusion coefficients in each of these three principal directions), that can only

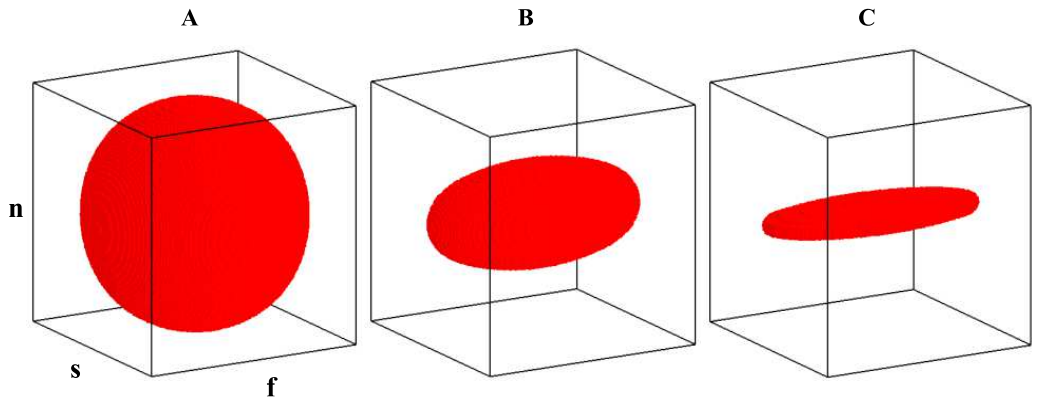

Figure 12: Snapshots of propagating wavefronts from a central spherical source in homogeneous 2 cm cubes of ten Tusscher-Noble-Noble-Panfilov endocardial human tissue [81]. (A) A spherical wavefront is obtained in isotropic tissue (A). In anisotropic tissue the wavefront is a prolate ellipsoid (B), while in orthotropic tissue it is a scalene ellipsoid (C)

be modelled in three dimensions, results in different wavefront geometries compared to isotropic or anisotropic propagation. The effects of introducing anisotropy and orthotropy of diffusion on the geometry of a propagating wavefront are illustrated in Fig. 12. The cubes are 2 cm slabs of endocardial ten Tusscher-Noble-Noble-Panfilov model [81] tissue with homogeneous myocyte orientations, with the Cartesian axes **f**, **s**, and **n** corresponding to the myocyte, sheet, and sheet normal directions, respectively. If diffusion is isotropic then diffusion and conduction velocity are identical in all directions and the shape of the propagating wavefront is spherical (Fig. 12A). If anisotropy of diffusion is introduced then propagation is fastest in the myocyte direction (**f**), but is equal in the sheet (**s**) and sheet normal (**n**) directions; thus the wavefront geometry is prolate ellipsoidal with the polar axis in the **f** direction (Fig. 12B). Reducing the diffusion coefficient in the sheet normal direction introduces orthotropy of diffusion; propagation is then different along the three principal axes, being fastest along the myocyte (**f**) and slowest in the sheet normal (**n**) direction, to give a wavefront geometry that is scalene ellipsoidal (Fig. 12C).

Because of these differences from one-dimensional propagation, and for completeness, the equations for three-dimensional propagation are presented here in full. To model two-dimensional media, the same equations can be

used but with any reference to the z or $\mathbf{n}$ directions removed (for example, in a two-dimensional medium the electrical diffusion tensor $\mathbf{D}$ in equation 65 will become a 2×2 tensor with four terms: D_{xx}, D_{xy}, D_{yx} and D_{yy}).

3.2.1. Reaction-diffusion equation in three dimensions

In three dimensions the reaction-diffusion equation is

$$\frac{\partial V}{\partial t} = \nabla(\mathbf{D}\nabla V) - I_{\text{ion}} \ , \tag{63}$$

where the spatial gradient operator ∇ is

$$\nabla = \frac{\partial}{\partial x} + \frac{\partial}{\partial y} + \frac{\partial}{\partial z} \ , \tag{64}$$

and $\mathbf{D}$ is an *electrical diffusion tensor*, a 3×3 symmetrical matrix:

$$\mathbf{D} = \begin{pmatrix} D_{xx} & D_{xy} & D_{xz} \\ D_{yx} & D_{yy} & D_{yz} \\ D_{zx} & D_{zy} & D_{zz} \end{pmatrix} \ . \tag{65}$$

Equation (63) can be written as a sum of doubly repeated indices [97] where we introduce the terms i and j to represent two of either x, y or z:

$$\frac{\partial V}{\partial t} = \sum_{i,j=x,y,z} \left[\frac{\partial}{\partial i} \left(D_{ij} \frac{\partial V}{\partial j} \right) \right] - I_{\text{ion}} \ . \tag{66}$$

The sum in three dimensions will have nine terms, as there are nine possible pair combinations of x, y and z. The sum in two dimensions will only have four terms as there are four possible pair combinations of x and y: (x, x), (x, y), (y, x) and (y, y).

3.2.2. Calculating the electrical diffusion tensor

Diffusion throughout the 3D heart (or a 2D sheet), and therefore the diffusion tensor $\mathbf{D}$, are functions of space and are determined by the tissue myocyte and sheet structure at any given point. The directions $\mathbf{f}$, $\mathbf{s}$ and $\mathbf{n}$ can be determined experimentally using histological methods, as for the Auckland canine cardiac geometry [98–100] and the San Diego rabbit cardiac geometry [101], or using diffusion tensor magnetic resonance imaging [18, 102, 103]

(see section 4.1). In a local coordinate system based on these vectors, the electrical diffusion tensor at a particular point in space is

$$\widetilde{\mathbf{D}} = \begin{pmatrix} D_{\parallel} & 0 & 0 \\ 0 & D_{\perp 1} & 0 \\ 0 & 0 & D_{\perp 2} \end{pmatrix} \ , \tag{67}$$

where $D_{\parallel}$ is electrical diffusion along the myocyte axis, $D_{\perp 1}$ is diffusion in the sheet plane perpendicular to the fibre axis, and $D_{\perp 2}$ is diffusion normal to the sheet plane (i.e. in the directions $\mathbf{f}$, $\mathbf{s}$ and $\mathbf{n}$, respectively). In order to find the components of the diffusion tensor $\mathbf{D}$ in the global Cartesian coordinate system, we must transform $\widetilde{\mathbf{D}}$ which uses a local coordinate system. As the three directions $\mathbf{f}$, $\mathbf{s}$ and $\mathbf{n}$ are the eigenvectors of the diffusion tensor $\mathbf{D}$ with corresponding eigenvalues $D_{\parallel}$, $D_{\perp 1}$ and $D_{\perp 2}$, then from linear algebra [97] the transformation matrix of $\widetilde{\mathbf{D}}$ to $\mathbf{D}$ is an orthogonal matrix

$$\mathbf{A} = (\mathbf{f}, \mathbf{s}, \mathbf{n}) \ , \tag{68}$$

where

$$\mathbf{f} = \begin{pmatrix} f_x \\ f_y \\ f_z \end{pmatrix} , \ \mathbf{s} = \begin{pmatrix} s_x \\ s_y \\ s_z \end{pmatrix} , \ \mathbf{n} = \begin{pmatrix} n_x \\ n_y \\ n_z \end{pmatrix} \ , \tag{69}$$

and where the subscripts x, y and z denote the components of the corresponding vectors with respect to the global Cartesian coordinate system. In this global Cartesian coordinate system the diffusion tensor $\mathbf{D}$ is then

$$\mathbf{D} = \mathbf{A}\widetilde{\mathbf{D}}\mathbf{A}^{\mathrm{T}} \ , \tag{70}$$

where the superscript T denotes matrix transpose. The matrices $\mathbf{A}$ and $\mathbf{A}^{\mathrm{T}}$ are the transformation matrices from the local to global coordinate systems and *vice versa*. Substitution of equation (68) into equation (70) then gives [104]

$$\mathbf{D} = D_{\parallel}\mathbf{f}\mathbf{f}^{\mathrm{T}} + D_{\perp 1}\mathbf{s}\mathbf{s}^{\mathrm{T}} + D_{\perp 2}\mathbf{n}\mathbf{n}^{\mathrm{T}} \ . \tag{71}$$

If it is assumed that diffusion perpendicular to the myocyte axis is the same in all directions (i.e. $D_{\perp 1} = D_{\perp 2}$) then equation (71) can be simplified [97, 104] using the fact that $\mathbf{A}$ is an orthogonal matrix such that

$$\mathbf{f}\mathbf{f}^{\mathrm{T}} + \mathbf{s}\mathbf{s}^{\mathrm{T}} + \mathbf{n}\mathbf{n}^{\mathrm{T}} = \mathbf{I} \ , \tag{72}$$

where

$$\mathbf{I} = \begin{pmatrix} 1 & 0 & 0 \\ 0 & 1 & 0 \\ 0 & 0 & 1 \end{pmatrix} \tag{73}$$

is the identity matrix. Substituting equation (72) into equation (71) then gives a representation of the electrical diffusion tensor $\mathbf{D}$ in terms of the vector describing myocyte axis orientation, $\mathbf{f}$, and the diffusion coefficients $D_{\parallel}$ and $D_{\perp 1}$:

$$\mathbf{D} = D_{\perp 1}\mathbf{I} + (D_{\parallel} - D_{\perp 1})\mathbf{f}\mathbf{f}^{\mathrm{T}} \ . \tag{74}$$

Therefore, for modelling anisotropic propagation where diffusion is the same in the sheet plane and across the sheet plane, the diffusion tensor can be calculated using equation (74). However, for modelling orthotropic propagation, where diffusion in the sheet plane and across the sheet plane is different, the diffusion tensor must be calculated using equation (71).

3.2.3. Calculating the diffusion term

The sum of the diffusion terms in equation (66) can now be calculated. The derivatives in the equation are expanded as follows

$$\frac{\partial}{\partial i}\left(D_{ij}\frac{\partial V}{\partial j}\right) = \frac{\partial D_{ij}}{\partial i}\frac{\partial V}{\partial j} + D_{ij}\frac{\partial^2 V}{\partial i \partial j} \ , \tag{75}$$

and so the sum term from equation (66) becomes

$$\sum_{i,j=x,y,z}\left[\frac{\partial}{\partial i}\left(D_{ij}\frac{\partial V}{\partial j}\right)\right] = \sum_{i,j=x,y,z}\left(\frac{\partial D_{ij}}{\partial i}\frac{\partial V}{\partial j}\right) + \sum_{i,j=x,y,z}\left(D_{ij}\frac{\partial^2 V}{\partial i \partial j}\right) \ . \tag{76}$$

Equation (66) can therefore be conveniently written as

$$\frac{\partial V}{\partial t} = S_1 + S_2 - I_{\mathrm{ion}} \ , \tag{77}$$

giving two sum terms, S_1 and S_2, that can be treated individually. For the first sum term, S_1, we expand as follows

$$S_1 = \sum_{i,j=x,y,z}\left(\frac{\partial D_{ij}}{\partial i}\frac{\partial V}{\partial j}\right) =$$

$$\frac{\partial D_{xx}}{\partial x}\frac{\partial V}{\partial x} + \frac{\partial D_{xy}}{\partial x}\frac{\partial V}{\partial y} + \frac{\partial D_{xz}}{\partial x}\frac{\partial V}{\partial z} + \frac{\partial D_{yx}}{\partial y}\frac{\partial V}{\partial x} + \frac{\partial D_{yy}}{\partial y}\frac{\partial V}{\partial y}$$

$$+ \frac{\partial D_{yz}}{\partial y}\frac{\partial V}{\partial z} + \frac{\partial D_{zx}}{\partial z}\frac{\partial V}{\partial x} + \frac{\partial D_{zy}}{\partial z}\frac{\partial V}{\partial y} + \frac{\partial D_{zz}}{\partial z}\frac{\partial V}{\partial z} \quad . \tag{78}$$

For the second sum term, S_2, we expand as follows, bearing in mind that the diffusion tensor $\mathbf{D}$ is symmetric (that is, $D_{xy} = D_{yx}$ and so on)

$$S_2 = \sum_{i,j=x,y,z} \left(D_{ij} \frac{\partial^2 V}{\partial i \partial j} \right) =$$

$$D_{xx}\frac{\partial^2 V}{\partial x^2} + D_{yy}\frac{\partial^2 V}{\partial y^2} + D_{zz}\frac{\partial^2 V}{\partial z^2}$$

$$+ 2\left(D_{xy}\frac{\partial^2 V}{\partial x \partial y} + D_{xz}\frac{\partial^2 V}{\partial x \partial z} + D_{yz}\frac{\partial^2 V}{\partial y \partial z} \right) \quad . \tag{79}$$

3.2.4. Discretisation scheme in three dimensions

We can now discretise the three dimensional reaction-diffusion equation (66) by taking discrete time steps Δt such that t at time step k is given by

$$t_k = t_0 + k\Delta t \qquad k = 0, 1, 2, \ldots, K \ , \tag{80}$$

and discrete space steps $\Delta x = \Delta y = \Delta z = h$ such that the point in space (x, y, z) at space step (l, m, n) is given by

$$x_l = x_0 + l \cdot h \qquad l = 0, 1, 2, \ldots, L \ , \tag{81}$$

$$y_m = y_0 + m \cdot h \qquad m = 0, 1, 2, \ldots, M \ , \tag{82}$$

$$z_n = z_0 + n \cdot h \qquad n = 0, 1, 2, \ldots, N \ . \tag{83}$$

The time derivative on the left-hand side of equation (66) is discretised using the Euler method as in equation (48). The derivatives in S_1 and S_2 (equations (78) and (79)) are approximated using central difference methods and values of V and D at time step k:

$$\frac{\partial V}{\partial x} = \frac{V^k_{(l+1,m,n)} - V^k_{(l-1,m,n)}}{2h} \ , \tag{84}$$

$$\frac{\partial V}{\partial y} = \frac{V^k_{(l,m+1,n)} - V^k_{(l,m-1,n)}}{2h} \ , \tag{85}$$

$$\frac{\partial V}{\partial z} = \frac{V^k_{(l,m,n+1)} - V^k_{(l,m,n-1)}}{2h} \ , \tag{86}$$

$$\frac{\partial^2 V}{\partial x^2} = \frac{V^k_{(l+1,m,n)} - 2V^k_{(l,m,n)} + V^k_{(l-1,m,n)}}{h^2} \ , \tag{87}$$

$$\frac{\partial^2 V}{\partial y^2} = \frac{V^k_{(l,m+1,n)} - 2V^k_{(l,m,n)} + V^k_{(l,m-1,n)}}{h^2} \ , \tag{88}$$

$$\frac{\partial^2 V}{\partial z^2} = \frac{V^k_{(l,m,n+1)} - 2V^k_{(l,m,n)} + V^k_{(l,m,n-1)}}{h^2} \ , \tag{89}$$

$$\frac{\partial^2 V}{\partial x \partial y} = \frac{V^k_{(l+1,m+1,n)} + V^k_{(l-1,m-1,n)} - V^k_{(l+1,m-1,n)} - V^k_{(l-1,m+1,n)}}{4h^2} \ , \tag{90}$$

$$\frac{\partial^2 V}{\partial x \partial z} = \frac{V^k_{(l+1,m,n+1)} + V^k_{(l-1,m,n-1)} - V^k_{(l+1,m,n-1)} - V^k_{(l-1,m,n+1)}}{4h^2} \ , \tag{91}$$

$$\frac{\partial^2 V}{\partial y \partial z} = \frac{V^k_{(l,m+1,n+1)} + V^k_{(l,m-1,n-1)} - V^k_{(l,m+1,n-1)} - V^k_{(l,m-1,n+1)}}{4h^2} \ , \tag{92}$$

$$\frac{\partial D_{xx}}{\partial x} = \frac{D_{xx(l+1,m,n)} - D_{xx(l-1,m,n)}}{2h} \ , \tag{93}$$

$$\frac{\partial D_{xy}}{\partial x} = \frac{D_{xy(l+1,m,n)} - D_{xy(l-1,m,n)}}{2h} \ , \tag{94}$$

$$\frac{\partial D_{xz}}{\partial x} = \frac{D_{xz(l+1,m,n)} - D_{xz(l-1,m,n)}}{2h} \ , \tag{95}$$

$$\frac{\partial D_{yx}}{\partial y} = \frac{D_{yx(l,m+1,n)} - D_{yx(l,m-1,n)}}{2h} \ , \tag{96}$$

$$\frac{\partial D_{yy}}{\partial y} = \frac{D_{yy(l,m+1,n)} - D_{yy(l,m-1,n)}}{2h} \ , \tag{97}$$

$$\frac{\partial D_{yz}}{\partial y} = \frac{D_{yz(l,m+1,n)} - D_{yz(l,m-1,n)}}{2h} \ , \tag{98}$$

$$\frac{\partial D_{zx}}{\partial z} = \frac{D_{zx(l,m,n+1)} - D_{zx(l,m,n-1)}}{2h} \ , \tag{99}$$

$$\frac{\partial D_{zy}}{\partial z} = \frac{D_{zy(l,m,n+1)} - D_{zy(l,m,n-1)}}{2h} \ , \tag{100}$$

$$\frac{\partial D_{zz}}{\partial z} = \frac{D_{zz(l,m,n+1)} - D_{zz(l,m,n-1)}}{2h} \ . \tag{101}$$

Using equations (48) and (84)-(101), the three dimensional reaction-diffusion equation (66) can be discretised and rearranged to give a solution for V at time step $k+1$.

3.3. Boundary conditions

Boundary conditions determine what happens to a variable of interest at the edge of a geometry, and generally take one of two forms in cardiac models: Euler or Neumann. For a one-dimensional cable, Euler (or cut-end) boundary conditions represent the cut end of a fibre where the potential is abolished, such that

$$V|_{x=0,L} = 0 \ , \tag{102}$$

and so in a discretisation scheme is simply implemented by setting $V = 0$ mV at $x = 0$ and $x = L$ (i.e. at each end of the fibre). Alternatively, Neumann (or no-flux) boundary conditions represent the experimental situation where the ends of a cut fibre or the edges of an extracted slice or slab of tissue seal over within a minute [105], or the physiologic boundaries of an *in vivo* or *ex vivo* tissue or organ, the entire ventricles for example. A such, Neumann boundary conditions are the appropriate choice for modelling cardiac tissue in the majority of situations. In a 1D model, Neumann boundary conditions represent a cable with sealed ends where the axial current is zero, and therefore

$$\left.\frac{\partial V}{\partial x}\right|_{x=0,L} = 0 \ . \tag{103}$$

In a discretisation scheme for a 1D model, Neumann boundary conditions are implemented using

$$\begin{aligned} V_0^{k+1} &= V_1^{k+1} \ , \\ V_L^{k+1} &= V_{L-1}^{k+1} \ . \end{aligned} \tag{104}$$

In 2D and 3D models, Neumann boundary conditions are implemented using

$$\left.\frac{\partial V}{\partial v}\right|_{\partial\Omega} = 0 \ , \tag{105}$$

where v is the exterior normal to the boundary $\partial\Omega$ of the two-dimensional medium R^2 or three-dimensional medium R^3, and where $\partial\Omega \subset R^2$ in 2D and $\partial\Omega \subset R^3$ in 3D. For a simple cuboid of dimensions $L \times M \times N$ space steps, this becomes

$$\left.\frac{\partial V}{\partial x}\right|_{x=0,L} = \left.\frac{\partial V}{\partial y}\right|_{y=0,M} = \left.\frac{\partial V}{\partial z}\right|_{z=0,Z} = 0 \ , \tag{106}$$

which in the discretisation scheme is implemented using

$$
\begin{aligned}
V^{k+1}_{(0,m,n)} = V^{k+1}_{(1,m,n)} \ , \quad V^{k+1}_{(L,m,n)} = V^{k+1}_{(L-1,m,n)} \quad \text{for all } m,n \ , \\
V^{k+1}_{(l,0,n)} = V^{k+1}_{(l,1,n)} \ , \quad V^{k+1}_{(l,M,n)} = V^{k+1}_{(l,M-1,n)} \quad \text{for all } l,n \ , \\
V^{k+1}_{(l,m,0)} = V^{k+1}_{(l,m,1)} \ , \quad V^{k+1}_{(l,m,N)} = V^{k+1}_{(l,m,N-1)} \quad \text{for all } l,m \ .
\end{aligned}
\tag{107}
$$

For irregular geometries such as whole ventricles or ventricular wedges, however, the implementation of boundary conditions is not so straightforward. The process involves finding the surface-normal vector for each node lying on the surface of the geometry. By assuming that the entire heart tissue is isopotential and at a different potential from outside the tissue, the fact that the current flow in an isotropic medium is normal to equipotential surfaces can be used to determine these surface normals [97, 106]. The node on the surface of (but inside) the tissue is then paired with its nearest-neighbour node lying outside the tissue and closest to the surface normal. Both are then assigned the same voltage, given for the node in the tissue by the reaction-diffusion PDE. An alternative algorithm based on the phase-field method, rather than calculating the surface normal, has also been suggested [107, 108].

3.4. Stability of the discretisation scheme

An important consideration when determining a differencing scheme for the reaction-diffusion PDE, in addition to the computational efficiency of the discretisation method, is the stability of the chosen method. von Neumann linear stability analysis [89] places constraints on the choice of Δt and Δx so that the stability criterion for any given discretisation scheme is

$$
D_{\parallel} \frac{\Delta t}{(\Delta x)^2} \leq \frac{1}{2d} \ , \tag{108}
$$

where d is the number of spatial dimensions. However, due to the stiff, nonlinear nature of the reaction-diffusion PDE and the biophysically detailed equations used to determine I_{ion}, this stability criterion is sometimes not sufficient; in such cases, the stability of the discretisation scheme can be checked by comparing the convergence of the solutions under variations of Δt and Δx.

3.5. Additional Methods for Integrating PDEs

The discretisation schemes presented in this chapter so far have all been Forward Time Centred Space explicit methods that, while being the simplest methods available and in terms of computational load are relatively undemanding, produce accurate numerical solutions. However, when working with biophysically detailed excitation equations that can have more than 20 differential equations and upwards of 100 algebraic equations to solve, and large geometries such as the whole ventricles that contain upwards of 10^6 nodes, it becomes necessary to utilise additional methods of integration in order to reduce computation time. In addition to the tabulation of exponential functions as described in section 2.9.4, the following methods may decrease computation time and increase tractability of computational simulations.

3.5.1. Operator splitting and adaptive time steps

As discussed in section 2.9.3, the integration time of single cardiac cell ODEs could be significantly reduced by applying an adaptive time step algorithm, where a small time step was used when the membrane potential was changing rapidly (e.g. during the phase 0 action potential upstroke) while a larger time step could be utilised when the membrane potential was changing more slowly. While applying such an adaptive time step algorithm would obviously be advantageous when solving the equations for simulations where total integration time is long-term and/or where large-scale geometries are being used, its direct application to the reaction-diffusion PDE is not straightforward. The problem of applying an adaptive time step algorithm arises because the diffusion component of the PDE must be calculated when all nodes in the tissue are at the same point in time. Using a large time step in a part of the tissue where the membrane potential is changing slowly will result in that part of the tissue moving forwards in time at a greater rate than a part of the tissue where a smaller time step is being utilised, and a disturbance to the synchronisation of time arises between nodes throughout the tissue. However, the technique of operator splitting [89] can be applied to the reaction-diffusion PDE to separate the reaction and the diffusion components, which can then be solved separately, with an adaptive time step algorithm being applied to the reaction component. This technique has been verified for the one- and two-dimensional cardiac reaction-diffusion PDE by Qu & Garfinkel [109], and will be described here using their method. The

reaction-diffusion PDE in one-, two- or three-dimensional cardiac tissue is

$$\frac{\partial V}{\partial t} = \nabla(\mathbf{D}\nabla V) - I_{\text{ion}} \ , \tag{109}$$

where ∇ is the spatial gradient operator in one, two or three dimensions as appropriate. Now consider the analogous differential equation

$$\frac{\partial V}{\partial t} = (\Gamma_1 + \Gamma_2)V \ , \tag{110}$$

where Γ_1 and Γ_2 are differential operators for the diffusion and the reaction components, respectively. Equation (110) can be integrated approximately as

$$V(t + \Delta T) = e^{(\Gamma_1+\Gamma_2)\Delta T}V(t) \ , \tag{111}$$

where we use ΔT to denote a *maximum* time step for reasons described later. Using the operator splitting method [89] this equation can further be approximated as

$$V(t + \Delta T) = e^{\Gamma_1\Delta T/2}e^{\Gamma_2\Delta T}e^{\Gamma_1\Delta T/2}V(t) + O(\Delta T^3) \ . \tag{112}$$

To apply this method to integrate equation (109) in the interval $[t, t + \Delta T]$, we proceed using 3 integration steps per maximum time step ΔT as follows. In step 1 we use initial conditions at time t to integrate equation (109) for a time step of $\Delta T/2$ using only the diffusion component:

$$\frac{\partial V}{\partial t} = \nabla(\mathbf{D}\nabla V) \ , \qquad \text{for a time step } \Delta T/2 \ , \tag{113}$$

which is equivalent to applying the differential operator $e^{\Gamma_1\Delta T/2}$ to $V(t)$ in equation (112). For step 2, we use as initial conditions the conditions from the end of step 1, and integrate equation (109) for a time step ΔT using only the reaction component:

$$\frac{\partial V}{\partial t} = -I_{\text{ion}} \ , \qquad \text{for a time step } \Delta T \ , \tag{114}$$

where the state variables (gating, ionic concentrations etc.) in the equations describing I_{ion} are also updated. This is equivalent to applying the differential operator $e^{\Gamma_2\Delta T}$ to the term $e^{\Gamma_1\Delta T/2}V(t)$ in equation (112). For step 3 we again

integrate equation (109) for a time step of $\Delta T/2$ using only the diffusion component, this time using the results of step 2 as initial conditions:

$$\frac{\partial V}{\partial t} = \nabla(\mathbf{D}\nabla V) \ , \qquad \text{for a time step } \Delta T/2 \ , \tag{115}$$

which is equivalent to applying the differential operator $e^{\Gamma_1 \Delta T/2}$ to the $e^{\Gamma_2 \Delta T} e^{\Gamma_1 \Delta T/2} V(t)$ term in equation (112). This step completes the integration of equation (109) in the interval $[t, t+\Delta T]$, and t then takes on the value $t+\Delta T$ before the three steps are repeated over the next time step ΔT. The advantage of using this operator splitting method is that we can now apply an adaptive time step algorithm during step 2, as there is no diffusion component to solve during this step and so, as long as all nodes are integrated for a total time ΔT, the time synchrony between nodes during the step is irrelevant. As the majority of computations (i.e. the stiff, high-order membrane excitation equations) are carried out during step 2, the application of an adaptive time step algorithm here dramatically decreases computation time. A *minimum* time step $\Delta t_{\min}$ must be chosen so that $\Delta T/\Delta t_{\min}$ is an integer in order to keep all nodes synchronised at the end of step 2, and so that integration of the equations describing I_{ion} is accurate. The maximum time step ΔT is chosen bearing in mind numerical stability of the integration, and is generally checked for by comparing convergence of solutions under variation of ΔT. The actual time step used during step 2, Δt, is then some integer multiple of $\Delta t_{\min}$ up to a maximum of $\Delta t = \Delta T$. Qu & Garfinkel [109] suggested an adaptive time step algorithm where $\Delta t_{\min} = 0.01$ ms and ΔT was set up to 0.4 ms for one-dimensional simulations and up to 0.3 ms for two-dimensional simulations. Δt was then determined according to $\Delta t = \Delta T/k$ where $k = k_0 + \text{int}(|\partial V/\partial t|)$ and where $k_0 = 5$ if $\partial V/\partial t > 0$ else $k_0 = 1$, in order to set up a protective zone to maintain safe propagation of any excitation wavefront. Finally, if $k > \Delta T/\Delta t_{\min}$ then $k = \Delta T/\Delta t_{\min}$. However, any adaptive time step algorithm that integrates the cellular membrane excitation equations accurately can be utilised.

3.5.2. Parallelisation under openMP and MPI

Because of the large spatial and temporal scales of cardiac simulations, and the limitations in terms of the computing power of single processors, it is necessary that computer codes are parallelised to run on multiple processors. Each processor then generally handles the equations needed to solve excitation and propagation in a specific subsection of the geometry, with communi-

cation between processors necessary for calculating the diffusion terms at the boundaries of each smaller geometry. Two of the most important standards for parallelisation of computer codes are openMP (open multi processing) and MPI (message passing interface).

openMP is a specification for parallelising codes for shared memory machines (where there are multiple processors but a single memory shared between all these processors) and takes the form of a set of compiler directives, library routines and environment variables for use with the C, C++ and Fortran computer programming languages. One advantage of using openMP is that the serial source code (e.g. a three-dimensional model) need not be considerably altered, and requires the placement in the code of directives that parallelise some form of looping construct such as a `for` loop.

MPI is an interface standard for parallelising codes for machines with a distributed memory architecture (where there are multiple processors each with its own memory). With these architectures it is necessary for processors to send and receive messages to and from other processors when determining the diffusion terms at the boundaries of their own local geometries. Implementing MPI requires that the source code be adapted to the specific needs of MPI, e.g. the programmer has to specifically define when messages will be sent and received, and is therefore not as straightforward as implementing openMP.

The exact implementation of openMP or MPI is dependent on the code being parallelised, and so a detailed description of the parallelisation of specific cardiac model codes is not given here other than to say that, in general, any construct such as a `for` statement that loops through the cardiac geometry can be parallelised. For more information on openMP and MPI see references [110, 111] or online at `http://www.openmp.org/` and `http://www.mpi-forum.org/`.

3.5.3. Parallelising irregular geometries

Parallelisation is usually undertaken by assigning a regular subsection of the total geometric area (e.g. a number of slices) to individual processors. If the tissue geometry is irregular, such as the whole ventricles, this regular assigning of space to processors may result in one processor solving equations for more tissue nodes than another processor – consider, for example, one processor handling the nodes in several apical slices of the geometry where relatively few nodes are inside the tissue, versus another processor handling nodes in the same number of basal slices where there are more nodes lying

in the tissue. This will reduce computation time as the processor with fewer tissue nodes waits for the other processors to calculate to the end of the time step (with parallelisation, each processor must be synchronised in time when the diffusion term of the reaction-diffusion PDE is calculated). In order to solve this problem, linear N element arrays containing the x, y and z locations of all nodes lying in the tissue can be created, with the elements of the arrays labelled $0 \ldots N-1$, where N is the total number of nodes in the tissue. Each processor is then assigned an equal number of these N nodes to solve equations for, with the x, y and z locations from the linear arrays allowing reference to the state variables for each node.

4. Experimental Data for Parameterising and Validating Tissue-Level Cardiac Models

With a mathematical/computational framework in place to describe tissue-level cardiac electrophysiology, experimental data are required to fulfil two major purposes: parameterisation and validation. Parameterisation is the process of assigning values or functions to model parameters such as ion channel maximal conductances ($\bar{g}$) and kinetics (τ), and the components of the electrical diffusion tensor $\widetilde{\mathbf{D}}$ (i.e. values for $D_{\parallel}$, $D_{\perp 1}$ and $D_{\perp 2}$) [5, 112]. Validation is the process of checking that model outputs, such as action potential duration and conduction velocity, are acceptable with respect to those measured experimentally [24, 84, 113].

Experimental techniques used for parameterising and validating sub-cellular models of calcium handling are discussed in Part 1 of this two-part article (Colman et al., in this issue), while the use of ion channel and action potential data in constructing cell-level electrophysiology models are discussed in [112]. Here we briefly discuss two tissue-level imaging techniques used to parameterise and validate ventricular models, namely *ex vivo* diffusion tensor magnetic resonance imaging (DT-MRI) and optical imaging.

4.1. Diffusion Tensor Magnetic Resonance Imaging

Myocyte orientation and sheet structure throughout the ventricular myocardium is responsible for many of the phenomena associated with the function of the heart, including spread of electrical excitation during both normal sinus rhythm and arrhythmias [95]. Propagation of electrical activity is anisotropic, being fastest in the direction of the long axis of the myocyte due to the presence of gap junctions that are principally located at the ends

of the myocytes [114–116]. Where sheets are present, propagation is orthotropic, being slowest in the direction normal to the sheet plane [117]. The myocyte and sheet architecture throughout the ventricles could itself be a substrate for arrhythmias including ventricular tachycardia and fibrillation, and sudden cardiac death, as has been suggested in both experimental (e.g. [118–121]) and theoretical (e.g. [55, 122–124]) studies. Furthermore, fibre orientation can change during certain pathological conditions such as hypertrophy [125], ischaemic heart disease [126] and heart failure [124]. If one wishes to study these phenomena, it is therefore important to include accurate representations of the three-dimensional geometry (shape) and architecture (myocyte/sheet structure) of the ventricles into tissue-level models.

Previous studies characterising the structure of the myocardium have utilised histological techniques in order to determine both myocyte orientation [127–129] and sheet structure [96, 130], or polarised light microscopy for determining myocyte orientation [131]. Myocyte orientation is known to follow a transmural helical pattern such that the inclination of the myocytes with respect to the short axis of the heart (the "inclination angle", also referred to as the "helix angle") shifts from positive at the endocardium to negative at the epicardium, changing sign at the midwall. The meticulous study of LeGrice et al. [96] suggested an organisation of the myocytes at a higher level into a laminar structure with sheets approximately four myocytes thick, with these sheets separated by sheet cleavage planes. The cleavage planes ran radially from the endocardium to the epicardium and, when viewed in a long axis transmural plane, could be seen to shift from a base-apex direction near the apex through to an apex-base direction in basal regions. However, histological techniques, even if the tissue does not require fixing as for polarised light microscopy, require reconstruction of myocyte and sheet orientations from sections and therefore introduce problems of distortion and alignment, and it is difficult to reconstruct the three-dimensional orientation of a myocyte or sheet as only angles in the stack of cut planes can be directly measured. Furthermore, most datasets describing geometry and architecture obtained using histological methods – such as the Auckland canine model [98–100] and the San Diego rabbit model [101] – are spatially smoothed; as such, they may not allow one to study the role of abrupt changes in myocyte orientation in arrhythmogenesis, for example.

Diffusion tensor magnetic resonance imaging (DT-MRI) [132] has been developed as a non-destructive, high-throughput method to reconstruct in

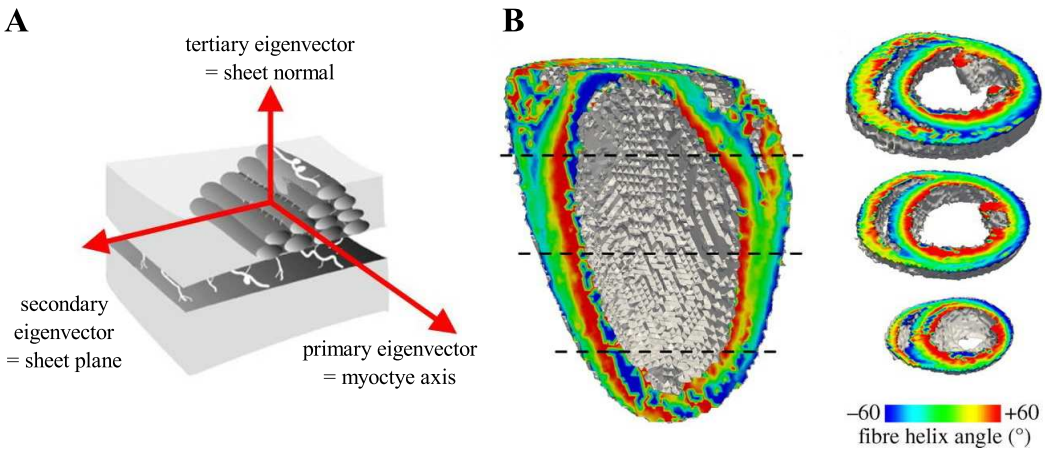

Figure 13: (A) Schematic of cardiac myocytes arranged into a laminar sheet structure. The arrows indicate how DT-MRI eigenvectors correspond to ventricular architecture. Adapted from [100]. (B) Maps of "fibre helix angle" (the inclination of the local myocyte axis with respect to the short axis of the heart) on a cut surface along the long axis of a rat heart (the grey surface is the endocardium of the left ventricle), and in three short axis slices taken from basal, equitorial and apical regions. From [18]

three-dimensions both the myocyte orientation and sheet structure throughout the ventricles. (The technique was originally applied to trace fibre tracts in the central nervous system [133–135], hence the common use of the term "fibre orientation" in the literature when DT-MRI is applied to the heart, even though "fibres" as such do not exist in the myocardium.) A detailed description of the DT-MRI technique is beyond the scope of this article, but interested readers are directed to reference [136]. Briefly, however, DT-MRI measures the diffusion of the proton (^{1}H) of water molecules (H_2O) in at least six different directions, at locations (voxels) throughout the sample of interest [137]. These directional diffusion data are then used to construct a 3×3 proton diffusion tensor at each voxel, that describes the three-dimensional diffusion of protons at that point in space. The eigenvectors and eigenvalues of the tensor are then calculated: these three eigenvectors correspond to the principal orthogonal directions of proton diffusion, with the associated eigenvalues quantifying the magnitude of the diffusion in those directions. The three eigenvectors are ranked as primary, secondary or tertiary ($\mathbf{v_1}$, $\mathbf{v_2}$ or $\mathbf{v_3}$, respectively) according to the magnitudes of their associated eigenvalues (λ_1, λ_2 and λ_3, respectively): the eigenvector with the largest eigenvalue is the

primary eigenvector, $\mathbf{v_1}$, while the tertiary eigenvector, $\mathbf{v_3}$, is the eigenvector with the smallest eigenvalue; the remaining eigenvector (with the intermediate eigenvalue) is the secondary eigenvector, $\mathbf{v_2}$.

Because cardiac myocytes have an elongated, rod-like shape [138], proton diffusion is greatest along the axis of the myocyte. As such, the primary eigenvector of the proton diffusion tensor corresponds to local myocyte orientation [139–141]. Where myocytes are organised into sheet-like structures, proton diffusion will be smallest normal to the sheet plane: therefore, as the three diffusion tensor eigenvectors are orthogonal, the secondary eigenvector corresponds to the direction perpendicular to the myocyte axis but lying in the sheet plane, while the tertiary eigenvector is normal to the sheet plane. As such, the secondary and tertiary eigenvectors give a measure of ventricular sheet structure [142, 143] (see Fig. 13A). Eigenvector orientations can therefore be quantified to give maps of myocyte and sheet structure throughout the myocardium (see Fig. 13B).

It follows from the above that the directions of the primary, secondary and tertiary DT-MRI eigenvectors ($\mathbf{v_1}$, $\mathbf{v_2}$ and $\mathbf{v_3}$) correspond to the vectors $\mathbf{f}$, $\mathbf{s}$ and $\mathbf{n}$, respectively, in equation (69), i.e. $\mathbf{v_1} = \mathbf{f}$, $\mathbf{v_2} = \mathbf{s}$ and $\mathbf{v_3} = \mathbf{n}$. Therefore, the DT-MRI eigenvectors can be used to calculate the electrical diffusion tensor (equation 65) in the PDE describing propagation of electrophysiological excitation (equation 63), through equation (70). However, although the DT-MRI eigenvectors (i.e. the principal directions of proton diffusion) relate to the vectors $\mathbf{f}$, $\mathbf{s}$ and $\mathbf{n}$ (i.e. the principal directions of local myocyte orientation), we are not aware of any data suggesting that the DT-MRI eigenvalues (i.e. the magnitudes of proton diffusion) relate to the parameters $D_{\parallel}$, $D_{\perp 1}$ and $D_{\perp 2}$ (i.e. the magnitudes of electrical diffusion). We therefore need additional experimental data to allow us to completely parameterise the electrical diffusion tensor $\mathbf{D}$ in equation (65).

4.2. Optical Imaging

Optical imaging (also known as optical mapping) of the heart can provide data to parameterise and partially validate cardiac tissue models. The application of voltage sensitive dyes to isolated and perfused cardiac tissue and hearts (using the Langendorff technique) allows the visualisation of spatio-temporal electrical activity, and has allowed the quantitative study of normal sinus rhythm and the organisation and development of cardiac arrhythmias (e.g. [26, 145]). As with the DT-MRI technique, a detailed description of

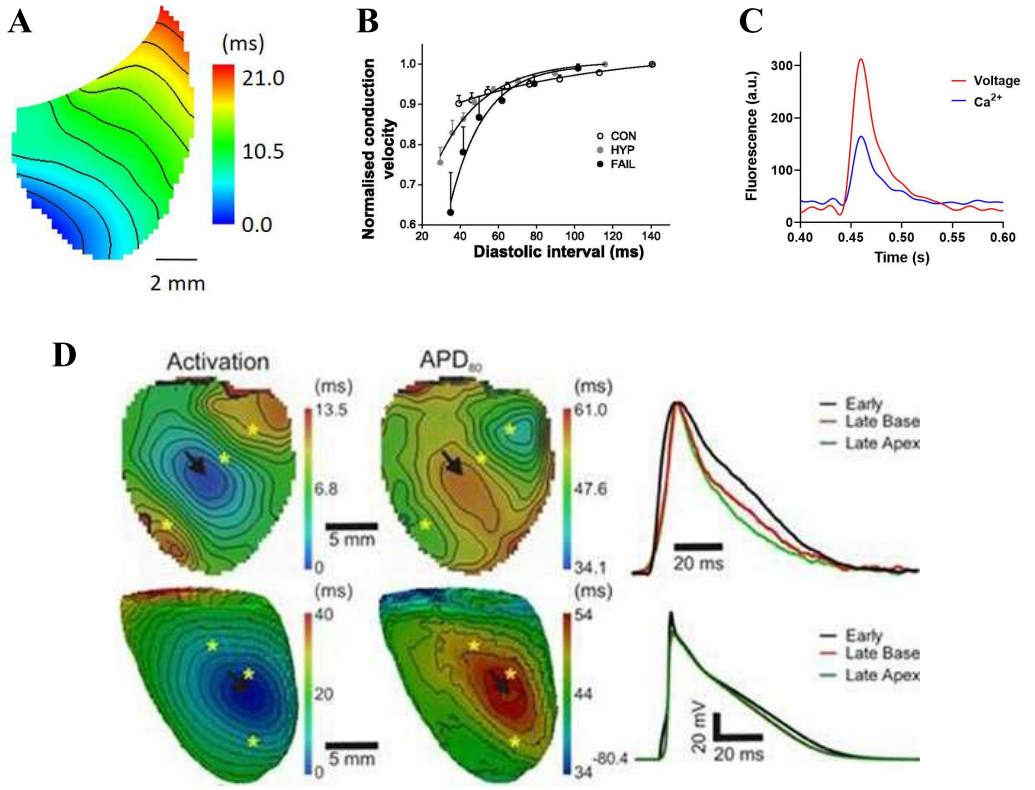

Figure 14: Optical imaging data used to parameterise and validate tissue-level cardiac electrophysiology models. (A) Colour-coded activation times across the right ventricular epicardial surface of an isolated perfused rat heart. (B) Optical imaging-derived conduction velocity restitution from healthy and diseased rat hearts: CON, control; HYP, hypertrophic; FAIL, failing. (C) Simultaneous optical imaging measurements of changes in membrane voltage (RH237 fluorescence) and intracellular Ca^{2+} (Rhod-2 fluorescence) from a 1 cm^2 area on the right ventricular epicardial surface of an isolated perfused rat heart, stimulated at a frequency of 5 Hz. (D) Optical imaging experiment outputs for a single rat heart (top panels) and the corresponding simulation outputs for a "heart-specific" model built using DT-MRI and optical imaging data from the heart in the top panels (bottom panels). Panels left to right show activation times, action potential duration maps and action potential traces acquired from areas indicated by asterisks (aligned by activation times). Pacing was at the site indicated by the arrow. A quantitative and qualitative comparison of optical imaging data and simulation outputs can be used as a means of model validation. Panels A and B from [144], panel D from [19]

optical imaging is beyond the scope of this article, but the interested reader is referred to references [8, 146] for reviews and [147, 148] for technical details.

In order to obtain focussed images and maintain spatial alignment over time, contraction of the isolated perfused heart is usually blocked by an excitation-contraction decoupler, such as blebbistatin: this results in a stationary heart with a geometry similar to end diastole (this compromise should be accounted for when optical imaging data are interpreted). Voltage-sensitive dyes, such as RH237, can then be introduced through coronary flow in perfused tissue preparations, or by superfusion in smaller tissue samples. These voltage-sensitive dyes bind to cardiac cell membranes and respond to changes in membrane potential (i.e. the action potential) by changes in their excitation and emission spectra. Spatio-temporal data acquisition of fluorescence is usually achieved by photodiode arrays or charge-coupled device (CCD) cameras. Contemporary CCD cameras readily allow high sampling rates (2 kHz and more) combined with superior spatial resolution. In conventional epi-fluorescence imaging of a perfused heart, both the light source for excitation of the dye and the detector are aimed at the epicardial surface; although fluorescence is obtained from the epicardial surface, significant contributions to the fluorescent signal originate from deeper myocardial layers due to the optical scattering and absorptive properties of tissue with respect to visible light (see [8] for details). Nevertheless, the data obtained from optical imaging under a variety of pacing protocols – principally spatial maps of activation times, repolarisation times, action potential durations and their restitution, and conduction velocities and corresponding restitution (see Fig. 14A,B) – allows partial parameterisation of tissue-level electrophysiology models. For example, although conduction velocity data obtained with optical imaging does not give absolute values for the components of the model electrical diffusion tensor $\widetilde{\mathbf{D}}$ (i.e. $D_{\parallel}$, $D_{\perp 1}$ and $D_{\perp 2}$ in equation 67), values for these parameters can be scaled until the model conduction velocities (along and across the myocyte axis) match those recorded using optical imaging. A relatively recent development in optical imaging of the heart is the concurrent recording of membrane voltage and intracellular Ca^{2+}, through the simultaneous use of voltage- and Ca^{2+}-sensitive dyes (such as the Ca^{2+}-sensitive dye Rhod-2) with different excitation and emission spectra [149] (Fig. 14C). As with membrane potential data, the intracellular Ca^{2+} data obtained from optical imaging can be used to parameterise the Ca^{2+} handling aspects of the cell electrophysiology model being developed.

The same optical imaging data can also be used, in part, to validate

developed models. This is particularly the case when "heart-specific" models are constructed, where functional (electrophysiological) data from optical imaging and structural data from DT-MRI are collected from the same heart and these data used to construct a specific model [18] (Fig. 14D). Such models are especially useful, as they allow one to study heart-specific phenomena that may be attributable to, for example, sample-specific myocyte arrangements or electrotonic interactions [19]. In these situations, the qualitative and quantitative similarities between the experimental and simulated activation, repolarisation, action potential duration and conduction velocity maps provides a partial validation for the developed models – see Fig. 14D. In the case where both membrane voltage and intracellular Ca^{2+} are simultaneously mapped using optical imaging, the subsequent model validation places tighter constraints on the model, as two experimental measures must be simultaneously and consistently matched over both time and space.

5. Conclusions

Computational models of the heart (from cell-level models, through one-, two- and three-dimensional tissue-level simplifications, to biophysically-detailed three-dimensional models of the ventricles, atria or whole heart) allow the simulation of excitation and propagation of this excitation, and have provided remarkable insight into the normal and pathological functioning of the heart. In this article we have presented equations, along with discretisation and integration schemes, and some experimental methods that allow parameterisation and validation of tissue-level models, that can be used to simulate cardiac electrophysiological function at the cell and tissue levels. Open-source code covering the modelling presented in this article is available in the Multi-scale Cardiac Simulation Framework available from `http://www.physicsoftheheart.com/`.

6. Acknowledgements

Parts of this work were undertaken on ARC3, part of the High Performance Computing facilities at the University of Leeds, UK.

Funding: This work was supported by the British Heart Foundation [grant number PG/16/74/32374 to AB and EW]; the Medical Research Council [Special Training Fellowship in Biomedical Informatics G0701776 to AB and Strategic Skills Fellowship MR/M014967/1 to MC]; the University of

Leeds [Biomedical Sciences Demonstrator Studentship to HS-C]; and the Wellcome Trust [Early Career Researcher Fellowship to DW, through Institutional Strategic Support Fund 204825/Z/16/Z].

References

[1] D. Bers, Excitation-Contraction Coupling and Cardiac Contractile Force, second ed., Klewer Academic Publishers: Dordrecht, The Netherlands, 2001.

[2] D. Bers, Cardiac excitation-contraction coupling, Nature 415 (2002) 198–205.

[3] D. Eisner, J. Caldwell, K. Kistamás, A. Trafford, Calcium and excitation-contraction coupling in the heart, Circulation Research 121 (2017) 181–195.

[4] A. Panfilov, A. Holden, Computational Biology of the Heart, John Wiley and Sons: Chichester, UK, 1997.

[5] R. Clayton, O. Bernus, E. Cherry, H. Dierckx, F. Fenton, L. Mirabella, A. Panfilov, F. Sachse, G. Seemann, H. Zhang, Models of cardiac tissue electrophysiology: progress, challenges and open questions, Progress in Biophysics and Molecular Biology 104 (2010) 22–48.

[6] J. Jalife, Introduction to the series on computational approaches to cardiac arrhythmias: translation into diagnostics and therapy, Circuation Research 112 (2013) 831–833.

[7] N. Trayanova, K. Chang, How computer simulations of the human heart can improve anti-arrhythmia therapy, Journal of Physiology 3594 (2016) 2483–2502.

[8] R. Walton, O. Bernus, Towards depth-resolved optical imaging of cardiac electrical activity, Advances in Experimental Medicine and Biology 859 (2015) 405–423.

[9] D. Hooks, M. Trew, B. Caldwell, G. Sands, I. LeGrice, B. Smaill, Laminar arrangement of ventricular myocytes influences electrical behavior of the heart, Circulation Research 101 (2007) e103–e112.

[10] D. Noble, Y. Rudy, Models of cardiac ventricular action potentials: iterative interaction between experiment and simulation, Philosophical Transactions of the Royal Society A – Mathematical, Physical and Engineering Sciences 359 (2001) 1127–1142.

[11] P. Hunter, P. Robbins, D. Noble, The IUPS human physiome project, Pflügers Archiv – European Journal of Physiology 445 (2002) 1–9.

[12] D. Noble, Modeling the heart – from genes to cells to the whole organ, Science 295 (2002) 1678–1682.

[13] D. Noble, The rise of computational biology, Nature Reviews Molecular Cell Biology 3 (2002) 460–463.

[14] P. Hunter, T. Borg, Integration from proteins to organs: the Physiome Project, Nature Reviews Molecular Cell Biology 4 (2003) 237–243.

[15] S. Niederer, N. Smith, At the heart of computational modelling, Journal of Physiology 590 (2012) 1331–1338.

[16] P. Lamata, R. Casero, V. Carapella, S. Niederer, M. Bishop, J. Schneider, P. Kohl, V. Grau, Images as drivers of progress in cardiac computational modelling, Progress in Biophysics and Molecular Biology 115 (2014) 198–212.

[17] A. Lopez-Perez, R. Sebastian, J. Ferrero, Three-dimensional cardiac computational modelling: methods, features and applications, Biomedical Engineering Online 14 (2015) 35.

[18] A. Benson, M. Al-Owais, A. Holden, Quantitative prediction of the arrhythmogenic effects of de novo hERG mutations in computational models of human ventricular tissues, European Biophysics Journal 40 (2011) 627–639.

[19] R. Walton, A. Benson, M. Hardy, E. White, O. Bernus, Electrophysiological and structural determinants of electrotonic modulation of repolarization by the activation sequence, Frontiers in Physiology 4 (2013) 281.

[20] M. Colman, E. Perez Alday, A. Holden, A. Benson, Trigger vs. substrate: multi-dimensional modulation of QT-prolongation associated

arrhythmic dynamics by a hERG channel activator, Frontiers in Physiology 8 (2017) 757.

[21] D. Whittaker, H. Ni, A. Benson, J. Hancox, H. Zhang, Computational analysis of the mode of action of disopyramide and quinidine on hERG-linked short QT syndrome in human ventricles, Frontiers in Physiology 8 (2017) 759.

[22] J. Sundnes, B. Nielsen, K. Mardal, X. Cai, G. Lines, A. Tveito, On the computational complexity of the bidomain and the monodomain models of electrophysiology, Annals of Biomedical Engineering 34 (2006) 1088–1097.

[23] S. Krishnamoorthi, L. Perotti, N. Borgstrom, O. Ajijola, A. Frid, A. Ponnaluri, J. Weiss, Z. Qu, W. Klug, D. Ennis, A. Garfinkel, Simulation methods and validation criteria for modeling cardiac ventricular electrophysiology, PLoS One 9 (2014) e114494.

[24] P. Pathmanathan, R. Gray, Validation and trustworthiness of multiscale models of cardiac electrophysiology, Frontiers in Physiology 9 (2018) 106.

[25] O. Aslanidi, M. Al-Owais, A. Benson, M. Colman, C. Garratt, S. g, J. Greenwood, A. Holden, S. Kharche, E. Kinnell, E. Pervolaraki, S. Plein, J. Stott, H. Zhang, Virtual tissue engineering of the human atrium: modelling pharmacological actions on atrial arrhythmogenesis, European Journal of Pharmaceutical Sciences 46 (2012) 209–221.

[26] A. Glukhov, V. Fedorov, Q. Lou, V. Ravikumar, P. Kalish, R. Schuessler, N. Moazami, I. Efimov, Transmural dispersion of repolarization in failing and nonfailing human ventricle, Circulation Research 106 (2007) 981–991.

[27] C.-H. Luo, Y. Rudy, A dynamic model of the cardiac action potential. I. Simulations of ionic currents and concentration changes, Circulation Research 74 (1994) 1071–1096.

[28] D. Bartos, E. Grandi, C. Ripplinger, Ion channels in the heart, Comprehensive Physiology 5 (2015) 1423–14641.

[29] T. Hund, Y. Rudy, Rate dependence and regulation of action potential and calcium transient in a canine cardiac ventricular cell model, Circulation 110 (2004) 3168–3174.

[30] V. Maltsev, H. Sabbah, A. Undrovinas, Late sodium current is a novel target for amiodarone: studies in failing human myocardium, Journal of Molecular and Cellular Cardiology 33 (2001) 923–932.

[31] A. Zygmunt, G. Eddlestone, G. Thomas, V. Nesterenko, C. Antzelevitch, Larger late sodium conductance in M cells contributes to electrical heterogeneity in canine ventricle, American Journal of Physiology – Heart and Circulatory Physiology 281 (2001) H689–H697.

[32] G. Droogmans, B. Nilius, Kinetic properties of the cardiac T-type calcium channel in guinea pig, Journal of Physiology 419 (1989) 627–650.

[33] C. Balke, W. Rose, E. Marban, W. Wier, Macroscopic and unitary properties of physiological ion flux through T-type Ca^{2+} channels in guinea-pig heart cells, Journal of Physiology 456 (1992) 247–265.

[34] G. Vassort, J. Alvarez, Cardiac T-type calcium current: pharmacology and roles in cardiac tissues, Journal of Cardiovascular Electrophysiology 5 (1994) 376–393.

[35] M. Dong, X. Sun, A. Prinz, H.-S. Wang, Effect of simulated I_{to} on guinea pig and canine ventricular action potential morphology, American Journal of Physiology – Heart and Circulatory Physiology 291 (2006) H631–H637.

[36] D.-W. Liu, G. Gintant, C. Antzelevitch, Ionic bases for electrophysiological distinctions among epicardial, midmyocardial, and endocardial myocytes from the free wall of the canine left ventricle, Circulation Research 72 (1993) 671–687.

[37] M. Sanguinetti, N. Jurkiewicz, Two components of the cardiac delayed rectifier K^+ current. Differential sensitivity to block by class III antiarrhythmic agents, Journal of General Physiology 96 (1990) 195–215.

[38] D.-W. Liu, C. Antzelevitch, Characteristics of the delayed rectifier current (I_{Kr} and I_{Ks}) in canine epicardial, midmyocardial, and endocardial

myocytes. A weaker I_{Ks} contributes to the longer action potential of the M cell, Circulation Research 76 (1995) 351–365.

[39] C. Antzelevitch, G.-X. Yan, W. Shimizu, Transmural dispersion of repolarisation and arrhythmogenicity. The Brugada syndrome versus the long QT syndrome, Journal of Electrocardiology 32 (1999) 158–165.

[40] B. Alberts, D. Bray, J. Lewis, M. Raff, K. Roberts, J. Watson, Molecular Biology of the Cell, third ed., Garland: New York, NY, 1994.

[41] A. Hodgkin, A. Huxley, B. Katz, Measurement of current-voltage relations in the membrane of the giant axon of *Loligo*, Journal of Physiology 116 (1952) 424–448.

[42] A. Hodgkin, A. Huxley, Currents carried by sodium and potassium ions through the membrane of the giant axon of *Loligo*, Journal of Physiology 116 (1952) 449–472.

[43] A. Hodgkin, A. Huxley, The components of membrane conductance in the giant axon of *Loligo*, Journal of Physiology 116 (1952) 473–496.

[44] A. Hodgkin, A. Huxley, The dual effect of membrane potential on sodium conductance in the giant axon of *Loligo*, Journal of Physiology 116 (1952) 497–506.

[45] A. Hodgkin, A. Huxley, A quantitative description of membrane current and its application to conduction and excitation in nerve, Journal of Physiology 117 (1952) 500–544.

[46] J. Rinzel, Electrical excitability of cells, theory and experiment: review of the Hodgkin-Huxley foundation and an update, Bulletin of Mathematical Biology 52 (1990) 5–23.

[47] C. Schwiening, A brief historical perspective: Hodgkin and Huxley, Journal of Physiology 590 (2012) 2571–2575.

[48] M. Boyett, A. Clough, J. Dekanski, A. Holden, Modelling cardiac excitation and excitability, in: A. Panfilov, A. Holden (Eds.), Computational Biology of the Heart, John Wiley and Sons: Chichester, UK, 1997, pp. 1–47.

[49] J. Keener, J. Sneyd, Mathematical Physiology, Springer-Verlag: New York, NY, 1998.

[50] R. FitzHugh, Thresholds and plateaus in the Hodgkin-Huxley nerve equations, Journal of General Physiology 43 (1960) 867–896.

[51] R. FitzHugh, Impulses and physiological states in theoretical models of nerve membrane, Biophysical Journal 1 (1961) 445–466.

[52] R. FitzHugh, Mathematical models of excitation and propagation in nerve, in: H. Schwan (Ed.), Biological Engineering, McGraw-Hill: New York, NY, 1969, pp. 1–85.

[53] J. Nagumo, S. Animoto, S. Yoshizawa, An active pulse transmission line simulating nerve axon, Proceedings of the Institute of Radio Engineers 50 (1962) 2061–2070.

[54] R. Aliev, A. Panfilov, A simple two-variable model of cardiac excitation, Chaos, Solitons and Fractals 7 (1996) 293–301.

[55] F. Fenton, A. Karma, Vortex dynamics in three-dimensional continuous myocardium with fiber rotation: Filament instability and fibrillation, Chaos 8 (1998) 20–47.

[56] M. Fink, D. Noble, Markov models for ion channels: versatility versus identifiability and speed, Philosophical Transactions of the Royal Society A – Mathematical, Physical and Engineering Sciences 367 (2009) 2161–2179.

[57] M. Stern, L. Song, H. Cheng, J. Sham, H. Yang, K. Boheler, E. Rios, Local control models of cardiac excitation-contraction coupling. A possible role for allosteric interactions between ryanodine receptors, Journal of General Physiology 113 (1999) 469–489.

[58] C. Clancy, Y. Rudy, Linking a genetic defect to its cellular phenotype in a cardiac arrhythmia, Nature 400 (1999) 566–569.

[59] C. Clancy, Y. Rudy, Cellular consequences of HERG mutations in the long QT syndrome: precursors to sudden cardiac death, Cardiovascular Research 50 (2001) 301–313.

[60] C. Clancy, Y. Rudy, Na^+ channel mutation that causes both Brugada and long-QT syndrome phenotypes: a simulation study of mechanism, Circulation 105 (2002) 1208–1213.

[61] T. Shannon, F. Wang, J. Puglisi, C. Weber, D. Bers, A mathematical treatment of integrated Ca dynamics within the ventricular myocytes, Biophysical Journal 87 (2004) 3351–3371.

[62] J. Silva, Y. Rudy, Subunit interaction determines I_{Ks} participation in cardiac repolarization and repolarization reserve, Circulation 112 (2005) 1384–1391.

[63] J. Balser, D. Roden, P. Bennett, Global parameter optimization for cardiac potassium channel gating models, Biophysical Journal 57 (1990) 433–444.

[64] C. Stevens, Interactions between intrinsic membrane protein and electric field: an approach to studying nerve excitability, Biophysical Journal 22 (1978) 295–306.

[65] S. Matsuoka, N. Sarai, S. Kuratomi, K. Ono, A. Noma, Role of individual ionic current systems in ventricular cells hypothesized by a model study, Japanese Journal of Physiology 53 (2003) 105–123.

[66] M. Clerx, K. Beattie, D. Gavaghan, G. Mirams, Four ways to fit an ion channel model, Biophysical Journal in press (2019) https://doi.org/10.1016/j.bpj.2019.08.001.

[67] T. O'Hara, L. Virág, A. Varró, Y. Rudy, Simulation of the undiseased human cardiac ventricular action potential: model formulation and experimental validation, PLoS Computational Biology 7 (2011) e1002061.

[68] D. Noble, Cardiac action and pacemaker potentials based on the Hodgkin-Huxley equations, Nature 188 (1960) 495–497.

[69] D. Noble, A modification of the Hodgkin-Huxley equations applicable to Purkinje fibre action and pacemaker potentials, Journal of Physiology 160 (1962) 317–352.

[70] H. Reuter, The dependence of the slow inward current in Purkinje fibres on the extracellular calcium concentration, Journal of Physiology 192 (1967) 479–492.

[71] D. Noble, R. Tsien, The kinetics and rectifier properties of the slow potassium current in cardiac Purkinje fibres, Journal of Physiology 195 (1968) 185–214.

[72] D. Noble, R. Tsien, Outward membrane currents activated in the plateau range of potentials in cardiac Purkinje fibres, Journal of Physiology 200 (1969) 205–231.

[73] R. McAllister, D. Noble, R. Tsien, Reconstruction of the electrical activity of cardiac Purkinje fibres, Journal of Physiology 251 (1975) 1–59.

[74] G. Beeler, H. Reuter, Reconstruction of the action potential of ventricular myocardial fibres, Journal of Physiology 268 (1977) 177–210.

[75] D. DiFrancesco, D. Noble, A model of cardiac electrical activity incorporating ionic pumps and concentration changes, Philosophical Transactions of the Royal Society B – Biological Sciences 307 (1985) 353–398.

[76] D. Hilgemann, D. Noble, Excitation-contraction coupling and extracellular calcium transients in rabbit atrium: reconstruction of basic cellular mechanisms, Proceedings of the Royal Society B 230 (1987) 163–205.

[77] C.-H. Luo, Y. Rudy, A model of the ventricular cardiac action potential. Depolarization, repolarization, and their interaction, Circulation Research 68 (1991) 1501–1526.

[78] C.-H. Luo, Y. Rudy, A dynamic model of the cardiac action potential. II. Afterdepolarizations, triggered activity, and potentiation, Circulation Research 74 (1994) 1097–1113.

[79] R. Amanfu, J. Saucerman, Modelling the effects of β_1-adrenergic receptor blockers and polymorphisms on cardiac myocyte Ca^{2+} handling, Molecular Pharmacology 86 (2014) 222–230.

[80] S. Cortassa, M. Aon, B. O'Rourke, R. Jacques, H.-J. Tseng, E. Marbán, R. Winslow, A computational model integrating electrophysiology, contraction, and mitochondrial bioenergetics in the ventricular myocyte, Biophysical Journal 91 (2006) 1564–1589.

[81] K. ten Tusscher, D. Noble, P. Noble, A. Panfilov, A model for human ventricular tissue, American Journal of Physiology 286 (2004) H1573–H1589.

[82] K. ten Tusscher, A. Panfilov, Alternans and spiral breakup in a human ventricular tissue model, American Journal of Physiology 291 (2006) H1088–H1100.

[83] E. Grandi, F. Pasqualini, D. Bers, A novel computational model of the human ventricular action potential and Ca transient, Journal of Molecular and Cellular Cardiology 48 (2010) 112–121.

[84] A. Carusi, K. Burrage, B. Rodríguez, Bridging experiments, models and simulations: an integrative approach to validation in computational cardiac electrophysiology, American Journal of Physiology – Heart and Circulatory Physiology 303 (2012) H144–H155.

[85] J. Rice, M. Jafri, Modelling calcium handling in cardiac cells, Philosophical Transactions of the Royal Society A – Mathematical, Physical and Engineering Sciences 359 (2001) 1143–1157.

[86] C. Soeller, M. Cannell, Analysing cardiac excitation-contraction coupling with mathematical models of local control, Progress in Biophysics and Molecular Biology 85 (2004) 141–162.

[87] R. Hinch, J. Greenstein, R. Winslow, Multi-scale models of local control of calcium induced calcium release, Progress in Biophysics and Molecular Biology 90 (2006) 136–150.

[88] H. Zhang, D. Noble, M. Cannell, C. Orchard, M. Lancaster, S. Jones, M. Boyett, A. Holden, M. Jafri, E. Sobie, W. Lederer, S. Demir, A. Michailova, F. Delprincipe, M. Egger, E. Niggli, G. Smith, C. Loughrey, N. MacQuaide, J. Dempster, A. Trafford, Dynamics of cardiac intracellular Ca^{2+} handling – from experiments to virtual cells, International Journal of Bifurcation and Chaos 13 (2003) 1–26.

[89] W. Press, S. Teukolsky, W. Vetterling, B. Flannery, Numerical Recipes in: The Art of Scientific Computing, third ed., Cambridge University Press: Cambridge, UK, 2007.

[90] S. Rush, H. Larsen, A practical algorithm for solving dynamic membrane equations, IEEE Transactions on Biomedical Engineering 25 (1978) 389–392.

[91] N. Trayanova, L. Rantner, New insights into defibrillation of the heart from realistic simulation studies, Europace 16 (2014) 705–713.

[92] J. Neu, W. Krassowska, Homogenization in syncytial tissues, Critical Reviews in Biomedical Engineering 21 (1993) 137–199.

[93] J. Jack, D. Noble, R. Tsien, Electric current flow in excitable cells, Oxford University Press: Oxford, UK, 1975.

[94] V. Fast, A. Kléber, Role of wavefront curvature in propagation of cardiac impulse, Cardiovascular Research 33 (1997) 258–271.

[95] A. Kléber, Y. Rudy, Basic mechanisms of cardiac impulse propagation and associated arrhythmias, Physiological Reviews 84 (2004) 431–488.

[96] I. LeGrice, B. Smaill, L. Chai, S. Edgar, J. Gavin, P. Hunter, Laminar structure of the heart: ventricular myocyte arrangement and connective tissue architecture in the dog, American Journal of Physiology – Heart and Circulatory Physiology 269 (1995) H571–H582.

[97] A. Panfilov, Modelling of re-entrant patterns in an anatomical model of the heart, in: A. Panfilov, A. Holden (Eds.), Computational Biology of the Heart, John Wiley and Sons: Chichester, UK, 1997, pp. 259–276.

[98] P. Hunter, P. Nielsen, B. Smaill, L. I.J., I. Hunter, An anatomical heart model with applications to myocardial activation and ventricular mechanics, in: T. Pilkington, B. Loftis, J. Thompson, S.-Y. Woo, T. Palmer, T. Budinger (Eds.), High-Performance Computing in Biomedical Research, CRC Press: Boca Raton, FL, 1993, pp. 3–26.

[99] P. Hunter, B. Smaill, P. Nielsen, I. LeGrice, A mathematical model of cardiac anatomy, in: A. Panfilov, A. Holden (Eds.), Computational Biology of the Heart, John Wiley and Sons: Chichester, UK, 1997, pp. 171–215.

[100] I. LeGrice, P. Hunter, A. Young, B. Smaill, The architecture of the heart: a data-based model, Philosophical Transactions of the Royal Society A – Mathematical, Physical and Engineering Sciences 359 (2001) 1217–1232.

[101] F. Vetter, A. McCulloch, Three-dimensional analysis of regional cardiac function: a model of rabbit ventricular anatomy, Progress in Biophysics and Molecular Biology 69 (1998) 157–183.

[102] S. Gilbert, A. Benson, P. Li, A. Holden, Regional localisation of left ventricular sheet structure: integration with current models of cardiac fibre, sheet and band structure, European Journal of Cardio-thoracic Surgery 32 (2007) 231–249.

[103] A. Benson, S. Gilbert, P. Li, S. Newton, A. Holden, Reconstruction and quantification of diffusion tensor imaging-derived cardiac fibre and sheet structure in ventricular regions used in studies of excitation propagation, Mathematical Modelling of Natural Phenomena 3 (2008) 101–130.

[104] L. Leon, B. Horáček, Computer model of excitation and recovery in the anisotropic myocardium. I. Rectangular and cubic arrays of excitable elements, Journal of Electrocardiology 24 (1991) 1–15.

[105] W. DeMello, The healing over process in cardiac and other muscle fibres, in: W. DeMello (Ed.), Electrical Phenomena in the Heart, Academic Press: New York, NY, 1972, pp. 323–351.

[106] A. Panfilov, J. Keener, Re-entry in an anatomical model of the heart, Chaos, Solitons and Fractals 5 (1995) 681–689.

[107] F. Fenton, E. Cherry, A. Karma, W.-J. Rappel, Modeling wave propagation in realistic heart geometries using the phase-field method, Chaos 15 (2005) 013502.

[108] A. Bueno-Orovio, V. Pérez-García, F. Fenton, Spectral methods for partial differential equations in irregular domains: the spectral smoothed boundary method, SIAM Journal on Scientific Computing 28 (2006) 886–900.

[109] Z. Qu, A. Garfinkel, An advanced algorithm for solving partial differential equation in cardiac conduction, IEEE Transactions on Biomedical Engineering 46 (1999) 1166–1168.

[110] B. Chapman, G. Jost, R. van der Pas, Using OpenMP: Portable Shared Memory Parallel Programming, The MIT Press: Cambridge, MA, 2008.

[111] P. Pacheco, Parallel Programming with MPI, Morgan Kaufmann Publishers, Inc: San Francisco, CA, 1997.

[112] S. Dokos, N. Lovell, Parameter estimation in cardiac ionic models, Progress in Biophysics and Molecular Biology 85 (2004) 407–431.

[113] S. Niederer, E. Kerfoot, A. Benson, M. Bernabeu, O. Bernus, C. Bradley, E. Cherry, R. Clayton, F. Fenton, A. Garny, E. Heidenreich, S. Land, M. Maleckar, P. Pathmanathan, G. Plank, J. Rodríguez, I. Roy, F. Sachse, G. Seemann, O. Skavhaug, N. Smith, Verification of cardiac tissue electrophysiology simulators using an N-version benchmark, Philosophical Transactions of the Royal Society A – Mathematical, Physical and Engineering Sciences 369 (2011) 4331–4351.

[114] L. Davis, H. Kanter, E. Beyer, J. Saffitz, Distinct gap junction protein phenotypes in cardiac tissues with disparate conduction properties, Journal of the American College of Cardiology 24 (1994) 1124–1132.

[115] J. Saffitz, M. Lloyd, B. Darrow, H. Kanter, J. Laing, E. Beyer, The molecular basis of anisotropy: role of gap junctions, Journal of Cardiovascular Electrophysiology 6 (1995) 498–510.

[116] K. Willecke, J. Eiberger, J. Degen, D. Eckhardt, A. Romualdi, M. Guldenagel, U. Deutsch, G. Sohl, Structural and functional diversity of connexion genes in the mouse and human genome, Biological Chemistry 383 (2002) 725–737.

[117] B. Caldwell, M. Trew, G. Sands, D. Hooks, I. LeGrice, B. Smaill, Three distinct directions of intramural activation reveal nonuniform side-to-side electrical coupling of ventricular myocytes, Circulation: Arrhythmia and Electrophysiology 2 (2009) 433–440.

[118] R. Myerburg, K. Kessler, A. Castellanos, Sudden cardiac death. structure, function, and time-dependence of risk, Circulation 85 (1992) I2–I10.

[119] R. Thakur, G. Klein, C. Sivaram, M. Zardini, D. Schleinkofer, H. Nakagawa, R. Yee, W. Jackman, Anatomic substrate for idiopathic left ventricular tachycardia, Circulation 93 (1996) 497–501.

[120] N. Tribulova, S. Novakova, A. Macsaliova, S. Sass, S. Thomas, S. Goetzfried, T. Podzuweit, M. Manoach, Histochemical and ultrastructural characterisation of an arrhythmogenic substrate in ischemic pig heart, Acta Histochemica 104 (2002) 393–397.

[121] J. de Bakker, M. Stein, H. van Rijen, Three-dimensional anatomic structure as substrate for ventricular tachycardia/ventricular fibrillation, Heart Rhythm 2 (2005) 777–779.

[122] J. Keener, A. Panfilov, The effects of geometry and fiber orientation on propagation and extracellular potentials in myocardium, in: A. Panfilov, A. Holden (Eds.), Computational Biology of the Heart, John Wiley and Sons: Chichester, UK, 1997, pp. 235–258.

[123] R. Clayton, A. Holden, Dynamics and interaction of filaments in a computational model of re-entrant ventricular fibrillation, Physics in Medicine and Biology 47 (2002) 1777–1792.

[124] D. Benoist, R. Stones, A. Benson, E. Fowler, M. Drinkhill, M. Hardy, D. Saint, O. Cazorla, O. Bernus, E. White, Systems approach to the study of stretch and arrhythmias in right ventricular failure induced in rats by monocrotaline, Progress in Biophysics and Molecular Biology 115 (2014) 162–172.

[125] P. Gosse, Left ventricular hypertrophy – the problem and possible solutions, Journal of International Medical Research 33 (2005) 3A–11A.

[126] R. Mazhari, J. Omens, J. Covell, A. McCulloch, Structural basis of regional dysfunction in acutely ischemic myocardium, Cardiovascular Research 47 (2000) 284–293.

[127] D. Streeter, H. Spotnitz, D. Patel, J. Ross, E. Sonnenblick, Fiber orientation in the canine left ventricle during diastole and systole, Circulation Research 24 (1969) 339–347.

[128] J. Ross, E. Sonnenblick, R. Taylor, H. Spotnitz, J. Covell, Diastolic geometry and sarcomere lengths in the chronically dilated canine left ventricle, Circulation Research 28 (1971) 49–61.

[129] D. Streeter, Gross morphology and fiber geometry of the heart, in: R. Berne, N. Sperelakis, S. Geiger (Eds.), Handbook of Physiology, Section 2: The Cardiovascular System, Volume 1: The Heart, American Physiological Society: Bethesda, MD, 1979, pp. 61–112.

[130] J. Chen, W. Liu, H. Zhang, L. Lacy, X. Yang, S.-K. Song, S. Wickline, X. Yu, Regional ventricular wall thickening reflects changes in cardiac fiber and sheet structure during contraction: quantification with diffusion tensor MRI, American Journal of Physiology – Heart and Circulatory Physiology 289 (2005) H1898–H1907.

[131] P.-S. Jouk, Y. Usson, G. Michalowicz, L. Grossi, Three-dimensional cartography of the pattern of the myofibres in the second trimester fetal human heart, Anatomy and Embryology 202 (2000) 103–118.

[132] P. Basser, J. Mattiello, D. LeBihan, MR diffusion tensor spectroscopy and imaging, Biophysical Journal 66 (1994) 259–267.

[133] C. Pierpaoli, P. Jezzard, P. Basser, A. Barnett, G. DiChiro, Diffusion tensor MR imaging of the human brain, Radiology 201 (1996) 637–648.

[134] V. Gulani, G. Iwamoto, H. Jiang, J. Shimony, A. Webb, P. Lauterbur, A multiple echo pulse sequence for diffusion tensor imaging and its application in excised rat spinal cords, Magnetic Resonance in Medicine 38 (1997) 868–873.

[135] B. Inglis, L. Yang, E. Wirth, P. Plant, T. Mareci, Diffusion anisotropy in excised normal rat spinal cord measured by NMR microscopy, Magnetic Resonance Imaging 15 (1997) 441–450.

[136] S. Mori, J.-D. Tournier, Introduction to Diffusion Tensor Imaging and Higher Order Models, second ed., Academic Press: Oxford, UK, 2014.

[137] I. Teh, R. Burton, D. McClymont, R. Capel, D. Aston, P. Kohl, J. Schneider, Mapping cardiac microstructure of rabbit heart in different mechanical states by high resolution diffusion tensor imaging: A proof-of-principle study, Progress in Biophysics and Molecular Biology 121 (2016) 85–96.

[138] S. Bird, P. Doevendans, M. van Rooijen, A. Brutel de la Riviere, R. Hassink, R. Passier, C. Mummery, The human adult cardiomyocyte phenotype, Cardiovascular Research 58 (2003) 423–434.

[139] E. Hsu, A. Muzikant, S. Matulevicius, R. Penland, C. Henriquez, Magnetic resonance myocardial fiber-orientation mapping with direct histological correlation, American Journal of Physiology – Heart and Circulatory Physiology 247 (1998) H1627–H1634.

[140] D. Scollan, A. Holmes, R. Winslow, J. Forder, Histological validation of myocardial microstructure obtained from diffusion tensor magnetic resonance imaging, American Journal of Physiology – Heart and Circulatory Physiology 275 (1998) H2308–H2318.

[141] A. Holmes, D. Scollan, R. Winslow, Direct histological validation of diffusion tensor MRI in formaldehyde-fixed myocardium, Magnetic Resonance in Medicine 44 (2000) 157–161.

[142] W.-Y. Tseng, V. Wedeen, T. Reese, R. Smith, E. Halpern, Diffusion tensor MRI of myocardial fibers and sheets: correspondence with visible cut-face texture, Journal of Magnetic Resonance Imaging 17 (2003) 31–42.

[143] P. Helm, H.-J. Tseng, L. Younes, E. McVeigh, R. Winslow, Ex vivo 3D diffusion tensor imaging and quantification of cardiac laminar structure, Magnetic Resonance in Medicine 54 (2005) 850–859.

[144] D. Benoist, R. Stones, M. Drinkhill, A. Benson, Z. Yang, C. Cassan, S. Gilbert, D. Saint, O. Cazorla, D. Steele, O. Bernus, E. White, Cardiac arrhythmia mechanisms in rats with heart failure induced by pulmonary hypertension, American Journal of Physiology – Heart and Circulatory Physiology 302 (2011) H2381–H2395.

[145] K. Nanthakumar, J. Jalife, S. Massé, E. Downar, M. Pop, J. Asta, H. Ross, V. Rao, S. Mironov, E. Sevaptsidis, J. Rogers, G. Wright,

R. Dhopeshwarkar, Optical mapping of langendorff-perfused human hearts: establishing a model for the study of ventricular fibrillation in humans, American Journal of Physiology – Heart and Circulatory Physiology 293 (2007) H875–H880.

[146] I. Efimov, V. Nikolski, G. Salama, Optical imaging of the heart, Circulation Research 95 (2004) 21–33.

[147] D. Rosenbaum, J. Jalife, Optical Mapping of Cardiac Excitation and Arrhythmias, Futura: Armonk, NY, 2001.

[148] M. Canepari, D. Zecevic, O. Bernus, Membrane Potential Imaging in the Nervous System and Heart, Springer: Cham, Switzerland, 2015.

[149] T. Herron, P. Lee, J. Jalife, Optical imaging of voltage and calcium in cardiac cells & tissues, Circulation Research 110 (2012) 609–623.